Pressure-dependent threshold in a granular flow: numerical modelling and experimental validation

Laurent Chupin, Thierry Dubois, Minh Phan, Olivier Roche

Pressure-dependent threshold in a granular flow: numerical modelling and experimental validation

Laurent Chupin[*], Thierry Dubois[*], Minh Phan[*], Olivier Roche[†]

May 4, 2020

Abstract

In an effort to model dry and dense granular flows, two viscoplastic models with constant viscosity and pressure-dependent thresholds are investigated through numerical simulations of the collapse of columns of glass beads over a horizontal plane. The yield stress in the Drucker-Prager model is proportional to the dynamic pressure, while that of the hydrostatic pressure model depends on the flow height. Unlike the Drucker-Prager model, which may lead to small-scale instabilities, the hydrostatic pressure model is well-posed. Both models are used to simulate the spreading of granular columns, with aspect ratios equal to 0.7 and 2, and comparison with experiments are presented. A level-set formulation for the Navier-Stokes equations is used, so that the interface between the granular material and the ambient air is tracked. The rheology is formulated as a projection, allowing for an efficient computation of the plastic part of the stress tensor. Coulomb friction conditions are applied on the walls. The dynamics of the collapse and the final deposit are accurately simulated with the Drucker-Prager model while the hydrostatic pressure model produces non-physically relevant solutions. The sensitivity of the results, with respect to the resolution, the viscosity, and the basal friction coefficient, is studied. During the collapse, the granular material consists of a basal deposit overlain by a flowing layer, which are separated by an interface that migrates upwards until the flowing layer is consumed. The time evolution of this static-mobile interface is quantified and a good agreement is found with experiments.

1 Introduction

Dense flows of dry granular matter are common phenomena in the environment and industry. Modeling these flows is essential for testing rheological laws that govern the motion of the granular material, and it is also important in the context of assessment of natural hazards or control of industrial processes. Various configurations have been considered over the last decades to better understand the behaviour of these flows (see the review GDR MiDi, 2004). Among them, the collapse of dense and dry columns of granular materials over a horizontal plane, also known as the dambreak configuration, has been extensively studied both experimentally and numerically (see, for a recent review, Delannay *et al.*, 2017). This configuration is particularly well-suited for testing numerical simulations against laboratory experiments, from which detailed data on flow kinematics and deposit morphology can be acquired. The behaviour of granular dambreak flows is well characterised. Once the granular column is released, the collapse, which lasts typically about one second in laboratory experiments, can be decomposed in four stages: a quick initial acceleration phase, followed by propagation of the front at constant velocity, further the flow decelerates and

[*]Laboratoire de Mathématiques Blaise Pascal, Université Clermont Auvergne and CNRS, Campus Universitaire des Cézeaux, 3 Place Vasarely, TSA 60026 – CS 60026, 63178 Aubière Cedex, France

[†]Laboratoire Magmas et Volcans, Université Clermont Auvergne-CNRS-IRD, OPGC, Campus Universitaire des Cézeaux, 6 Avenue Blaise Pascal, TSA 60026 – CS 60026, 63178 Aubière Cedex, France

finally, while the front has reached the runout (maximum) distance, the granular flow moves very slowly until it stops. The granular flows during the collapse are formed by a basal deposit, growing at a nearly constant rate, overlain by a moving part whose head slides on the bottom wall (Roche, 2012). During the last stage, once the front has stopped, the basal deposit still grows slowly until it reaches the top and front of the mass. This internal dynamics, characterised by a static-mobile interface between the deposit and the moving layer, is quantified from experiments (Roche, 2012). Also, the final deposit is characterised by its height, its runout distance, and its profile. Therefore, there are many available measured data on the collapse of granular flow, so that comparing numerical methods and/or different modelling approaches for this problem is appealing.

Numerical simulation of granular drambreak experiments are performed either by using depth-averaged models (see, for instance, Mangeney-Castelnau *et al.*, 2005; Kerswell, 2005; Larrieu *et al.*, 2006; Gueugneau *et al.*, 2017), Discrete Element Methods (see, for instance, Lacaze *et al.*, 2008; Girolami *et al.*, 2012) or two-dimensional continuum models (Crosta *et al.*, 2009; Lagrée *et al.*, 2011; Ionescu *et al.*, 2015; Martin *et al.*, 2017). Depth-averaged models are restricted to granular columns with aspect ratio less than unity and are not able to compute the dynamics of the static-mobile interface. Most of the above cited numerical studies focused on recovering scaling-laws that characterise the flow runout distance and that are provided by experiments (see, for instance Balmforth & Kerswell, 2005). In Ionescu *et al.* (2015) and Martin *et al.* (2017), detailed analyses of the flow dynamics and comparisons of numerical simulations with experiments (Mangeney *et al.*, 2010) have been first attempted. These studies rely on the use of continuum viscoplastic models: the $\mu(I)$-rheology (Jop & Pouliquen, 2006) and the Drucker-Prager (DP) model. These models share the same yield stress, which is proportional to the dynamic pressure, but they have different viscosities. The DP-model can be viewed as a constant viscosity version of the $\mu(I)$–rheology. The main advantage of the DP-model is that the only parameter that has to be adjusted is the viscosity while the $\mu(I)$–rheology depends on parameters that are not easily measurable. Note that developing a model with as less parameters as possible is advisable in a view to applying it to geophysical flows. Little differences were observed in Ionescu *et al.* (2015), for viscosities in the range $[0.1, 0.5]$ Pa s, for collapse over a horizontal plane. Also, both models predicted results in good agreement with experiments. Note that the numerical convergence of the results was not addressed in Ionescu *et al.* (2015) and Martin *et al.* (2017).

In this paper, we propose to go further than earlier studies in the numerical simulation of the collapse of granular columns with the DP-model by studying the numerical convergence, by estimating the influence of the viscosity and of the basal friction and by analysing the dynamics of the static-mobile interface. Two sets of experiments, which differ in the aspect ratio of the granular column and the size of the particles, are considered. The first one, with aspect ratio 0.7, was already studied by Ionescu *et al.* (2015) so that comparisons with their numerical results and with the experiment can be performed. Numerical results for the second experiment, which was carried out by Roche *et al.* (2010) and had an aspect ratio equals to 2, are presented for the first time. In the present study, the rheological parameters, namely the internal and basal friction coefficients, are prescribed from the experiments. We have developed an efficient parallel code, so that we were able to decrease the mesh size until the numerical convergence was obtained, which assessed the reliability of the results. The effect of the viscosity on the results could also be studied by decreasing its value down to 10^{-2} Pa s (ten times smaller than in Ionescu *et al.* (2015)).

While being able to reproduce the flow dynamics, models with DP yield stress are known to be mathematically ill–posed and are characterised by small–scale instabilities (see Schaeffer, 1987; Schaeffer & Pitman, 1988; Martin *et al.*, 2017). As shown in Chupin & Mathé (2017), replacing the dynamic pressure by a hydrostatic pressure (HP-model) in the yield stress leads to a well-posed model. The predictability of the HP-model has, up to now, never been investigated. One of the main objective of this paper is to evaluate the HP-model in the context of the collapse of granular columns. Simulations performed with the HP-model are also compared with the aforementioned

experiments.

In a viscoplastic rheology, the stress tensor is proportional to the strain-rate tensor when its strength is above the yield stress otherwise it is not prescribed. In order to handle this non-differentiable definition, a framework, which avoids the formalism of variational inequalities (Glowinsky *et al.*, 1981), was introduced in Chupin & Dubois (2016): it relies on a projection formulation for the definition of the plastic part of the stress tensor. By coupling this approach with classical fractional step methods to approximate solutions of the incompressible Navier-stokes equations (Guermond *et al.*, 2006), an efficient bi-projection scheme for the time discretisation of Bingham equations was proposed and studied in Chupin & Dubois (2016). Note that in this scheme, the plastic part of the stress tensor is computed with a fixed point procedure enjoying a geometrical convergence rate. The bi-projection scheme was further extended in Chalayer *et al.* (2018) to viscoplastic fluids with spatially variable viscosity, density and yield stress. A version adapted from Chalayer *et al.* (2018) is used in the present paper.

The surface of the granular mass during the collapse was treated as a free surface in Ionescu *et al.* (2015) and Martin *et al.* (2017), which means that the motion of the ambient medium was not computed. In this paper, we use the level-set method (Sussman *et al.*, 1994) to capture the interface between the granular mass and the ambient air. Interface tracking methods allow to handle a wider variety of problems and to use simple and efficient algorithms on Cartesian grids. In the level-set approach the interface is the set of zeros of a smooth function advected by the velocity field. However, for dambreak problems, the level-set method is known to encounter difficulties in accurately predicting the angle between the interface and a wall (Della Rocca & Blanquart, 2014) and therefore the correct propagation of the front. We show in this paper that reducing the order of the schemes in the neighbourhood of a boundary without adding ghost points and implementing friction boundary conditions permits us to produce very accurate numerical results in the context of the collapse of granular columns. Note that an alternative to the level-set method is the Volume of Fluid method, which has been successfully used by Liu *et al.* (2016) to study viscoplastic dambreaks.

In this article, numerical simulations of the collapse of columns of glass beads, with aspect ratios 0.7 and 2, over horizontal plane are performed and compared with experimental results. Two continuum viscoplastic models with constant viscosity and pressure-dependent yield stress are considered. In section 2, the mathematical models as well as the complementary boundary conditions and definitions of the yield stress threshold are given. The numerical methods are summarised in section 3. The numerical results are analysed and compared with laboratory experiments in section 4. Two experiments are considered and they differ in the aspect ratio of the granular column and the size of the glass beads. The flow dynamics and the profile of the granular mass obtained with the DP-model are compared with experiment. Sensibilities of the numerical results upon the resolution, values of the constant viscosity and/or the basal friction coefficient are studied. For the second experiment, with an initial column with aspect ratio 2, numerical results are presented for the first time. In this case, the static-mobile interface, which characterises the internal dynamics of the granular flow, is analysed. For both experiments, simulations performed with the HP-model are presented.

2 Mathematical modeling

2.1 Conservation laws and rheology

We consider the collapse of a granular mass over a horizontal rigid surface. The mathematical model is written in two-dimension and involves two components: a viscoplastic part corresponding to the granular mass, and a newtonian part modelling the surrounding air. The flow is assumed to

be incompressible with variable density so that the mass and momentum conservation laws write

$$\rho\big(\partial_t \boldsymbol{u} + \boldsymbol{u}\cdot\boldsymbol{\nabla}\boldsymbol{u}\big) = \operatorname{div}\boldsymbol{T} + \rho\boldsymbol{g}, \tag{1}$$

$$\operatorname{div}\boldsymbol{u} = 0, \tag{2}$$

$$\partial_t \rho + \boldsymbol{u}\cdot\boldsymbol{\nabla}\rho = 0, \tag{3}$$

where $\boldsymbol{u}$ is the material velocity, $\boldsymbol{g}$ an external force (gravity), ρ the mass density, and $\boldsymbol{T}$ the total stress tensor. The rheology is defined by the viscoplastic law:

$$\boldsymbol{T} = -p\,\boldsymbol{Id} + 2\eta\,\boldsymbol{D}(\boldsymbol{u}) + \kappa\frac{\boldsymbol{D}(\boldsymbol{u})}{|\boldsymbol{D}(\boldsymbol{u})|}, \tag{4}$$

where p is the pressure, $\boldsymbol{D}(\boldsymbol{u}) = \frac{1}{2}\big(\boldsymbol{\nabla}\boldsymbol{u} + (\boldsymbol{\nabla}\boldsymbol{u})^t\big)$ is the strain rate tensor, η is the dynamic viscosity, and κ is the yield stress. Here, the norm is the modified Frobenius norm $|\boldsymbol{D}(\boldsymbol{u})|^2 = \frac{1}{2}\sum_{i,j}\boldsymbol{D}(\boldsymbol{u})_{ij}^2$. Note that when $\boldsymbol{D}(\boldsymbol{u}) = 0$ the equation (4) must be read: $\boldsymbol{T} = -p\,\boldsymbol{Id} + \boldsymbol{T'}$ where $\boldsymbol{T'}$ is any symmetric tensor such that $|\boldsymbol{T'}| \le \kappa$.
To take into account the presence of the two phases, we will assume that initially the density ρ takes exactly two constant values: that of the air ρ_{f} and that of the granular medium ρ_{s}. We will assume that this property will be satisfied throughout the experiment (from a numerical point of view, this property will be ensured using a level-set method). Obviously, both the viscosity and the yield stress also depend on ρ and may take two values:

$$\eta = \eta_{\mathrm{f}} \quad \text{and} \quad \kappa = 0 \qquad \text{if} \quad \rho = \rho_{\mathrm{f}}, \tag{5}$$

$$\eta = \eta_{\mathrm{s}} \quad \text{and} \quad \kappa = \tan(\alpha)\,p \qquad \text{if} \quad \rho = \rho_{\mathrm{s}}. \tag{6}$$

The constant η_{f} corresponds to the air dynamic viscosity, and we have chosen 0 as yield stress in the air since air is a Newtonian fluid and has no plastic behaviour. The viscosity η_{s} is taken constant in this work, but some works use a more complex pressure-dependent relationship (such as the $\mu(I)$-law). On the contrary, in the granular medium we use the Drucker–Prager law to describe the relationship between the yield and the pressure: $\tan(\alpha)$ is the static internal friction coefficient, with α the internal friction angle.
In some cases, it may be interesting to replace, in the expression of yield stress, the pressure p by a hydro-static pressure denoted p_{hyd} and depending on the weight above a point. This choice can be intuitive when considering thin flows or more generally when the flows are mainly driven by the pressure and the gravity forces: in that cases, the momentum equation (1) reduces to $\nabla p_{\mathrm{hyd}} = \rho g$. Consequently, we will also propose the following model instead of (6):

$$\eta = \eta_{\mathrm{s}} \quad \text{and} \quad \kappa = \tan(\alpha)\,p_{\mathrm{hyd}} \qquad \text{if} \quad \rho = \rho_{\mathrm{s}}, \tag{7}$$

where $p_{\mathrm{hyd}} = \displaystyle\int_z^{\mathrm{top}} \rho g$, with the value denoted "top" corresponds to the height of the granular mass. One of the objectives of this work is to compare the two possible rheologies (6) and (7). In the remaining of the paper, the model based on (6) will be named the DP-model while HP-model will be used to designate the one based on (7).

2.2 Boundary conditions

The equations (1)–(3) are completed with boundary conditions. Generally, the boundary $\partial\Omega$ of the domain Ω will be composed of two parts: $\partial\Omega_{\mathrm{a}}$ and $\partial\Omega_{\mathrm{w}}$ on which we will impose different conditions. The bound $\partial\Omega_{\mathrm{a}}$ will correspond to the part of the domain in the free air while the bound $\partial\Omega_{\mathrm{w}}$ will refer to solid walls.

In any case, we will note by $\boldsymbol{n}$ the outgoing unit normal to the domain. In practice, we decompose the velocity $\boldsymbol{u}$ at the boundary into normal velocity $u_n = \boldsymbol{u}\cdot\boldsymbol{n}$ and tangent velocity $\boldsymbol{u}_t = \boldsymbol{u} - u_n\boldsymbol{n}$. In the same way, we introduce the following notations for the stress: $T_n = (\boldsymbol{T}\cdot\boldsymbol{n})\cdot\boldsymbol{n}$ and $\boldsymbol{T}_t = \boldsymbol{T}\cdot\boldsymbol{n} - T_n\boldsymbol{n}$.
On the bound $\partial\Omega_{\rm a}$, the velocity field satisfies

$$u_n = 0 \quad \text{and} \quad \partial_n \boldsymbol{u}_t = 0. \tag{8}$$

On the back and bottom walls, we take into account the friction so that the boundary conditions must be written:

$$u_n = 0 \quad \text{and} \quad \boldsymbol{T}_t = -\eta_{\rm b}\boldsymbol{u}_t - \kappa_{\rm b}\,\frac{\boldsymbol{u}_t}{|\boldsymbol{u}_t|} \qquad \text{on } \partial\Omega_{\rm w}. \tag{9}$$

The coefficients $\eta_{\rm b}$ and $\kappa_{\rm b}$ depend on the density. More precisely, we impose

$$\eta_{\rm b} > 0 \quad \text{and} \quad \kappa_{\rm b} = 0 \qquad \text{if} \quad \rho = \rho_{\rm f}, \tag{10}$$

$$\eta_{\rm b} = 0 \quad \text{and} \quad \kappa_{\rm b} = \tan(\alpha_b)\,(-T_n)^+ \qquad \text{if} \quad \rho = \rho_{\rm s}. \tag{11}$$

The coefficient $\tan(\alpha_b)$ is called the Coulomb friction coefficient and α_b is the basal friction angle. As in the case of Bingham's law, when $\boldsymbol{u}_t = 0$ the second part of (9) must be read $|\boldsymbol{T}_t| \le \kappa_{\rm b}$.

Note that boundary condition (9) when applied to the part of $\partial\Omega_{\rm w}$ on which air (with $\kappa_{\rm b} = 0$) is sliding reduces to a Navier condition. Indeed, let us detail the particular case of the bottom wall for which we have $\boldsymbol{n} = (0,-1)^t$. Therefore $\boldsymbol{T}_t = (-\eta\partial_y u, 0)^t$ (indeed $\partial_x v = 0$ as $v = -u_n = 0$) so that (9) rewrites $-\eta\partial_y u + \eta_{\rm b} u = 0$. The main advantage of Navier conditions is that, depending upon the value of the parameter $\eta_{\rm b}$, it allows to impose Dirichlet ($\eta_{\rm b} = \infty$), mixed ($0 < \eta_{\rm b} < \infty$) or Neumann ($\eta_{\rm b} = 0$) boundary conditions. In most numerical simulations presented in the paper, the value $\eta_{\rm b} = 1$ will be used for air on the bottom boundary.

3 Numerical method

3.1 Level-set approach

The interface between the air and the granular medium is tracked with a level-set function ϕ, so that the interface Γ is the set of points where ϕ vanishes. The level-set function is a smooth function of $\boldsymbol{x}$: the signed distance function from the interface is commonly used; see Osher & Fedkiw (2003) and the reference therein. The physical density is smeared out at the interface, so that we define

$$\rho(\phi) = \rho_{\rm f} H_\epsilon(\phi) + \rho_{\rm s}(1 - H_\epsilon(\phi)), \tag{12}$$

where $H_\epsilon(\phi)$ is the regularised Heaviside function

$$H_\epsilon(\phi) = \begin{cases} 0 & \text{if } \phi < -\epsilon, \\ \frac{1}{2}\Big(1 + \frac{\phi}{\epsilon} + \sin\big(\frac{\pi\phi}{\epsilon}\big)/\pi\Big) & \text{if } |\phi| \le \epsilon, \\ 1 & \text{if } \phi > \epsilon. \end{cases}$$

The yield stress $\kappa(\phi)$ and the boundary coefficients $\eta_{\rm b}(\phi)$ and $\kappa_{\rm b}(\phi)$ are treated as a sharp discontinuity. In order to ensure continuity of the tangential shear stress, the viscosity $\eta(\phi)$ is a harmonic mean of $\eta_{\rm s}$ and $\eta_{\rm f}$

$$\frac{1}{\eta(\phi)} = \frac{\theta(\phi)}{\eta_{\rm s}} + \frac{(1-\theta(\phi))}{\eta_{\rm f}}$$

where the height fraction $\theta(\phi)$ is defined as in Sussman *et al.* (2007).

In the level-set formulation (see Sussman *et al.*, 1994; Chang *et al.*, 1996; Sussman *et al.*, 1998), ϕ is advected by the velocity so that mass conservation equation (3) is replaced by a transport equation. In this context, the level-set formulation modeling a column of granular medium sliding into ambient air writes

$$\partial_t \phi + \operatorname{div}(\boldsymbol{u}\phi) = 0, \tag{13}$$

$$\rho(\phi)\left(\partial_t \boldsymbol{u} + \operatorname{div}(\boldsymbol{u}\otimes\boldsymbol{u})\right) + \boldsymbol{\nabla} p = -\rho(\phi) g \boldsymbol{e}_2 + \operatorname{div}\left(2\eta(\phi)\boldsymbol{D}(\boldsymbol{u}) + \kappa(\phi)\boldsymbol{S}\right), \tag{14}$$

$$\operatorname{div}\boldsymbol{u} = 0, \tag{15}$$

where g is the gravitational constant, $\boldsymbol{e}_2$ is the vertical unit vector and $\boldsymbol{S}$ is the plastic part of the stress tensor that will be rigorously defined in section 3.2. Equations (13)-(15) are supplemented by the boundary conditions (8)-(9) where the friction coefficients depend on ϕ. Note that nonlinear terms are written in conservative form in level-set and momentum equations. Also, surface tension forces are not taken into account.

The transport equation (13) is discretised with a finite volume WENO scheme of order 5 (Shu & Osher, 1988; Jiang & Peng, 2000) in space combined with TVD RK3 scheme for the time discretisation (Gottlieb & Shu, 1998). Even if the discrete level-set function is initialised as the signed distance from the interface, it will not remain a distance function and, as it is suggested in Sussman *et al.* (1994), a redistancing algorithm needs to be applied periodically in time. A classical approach consists in solving numerically a Hamilton-Jacobi equation. Stationary solutions of the Hamilton-Jacobi equation are distance functions and share their interface with the level-set function. In this paper, the redistancing algorithm given by Min (2010) is used. It relies on a TVD RK2 method as time marching scheme and on a ENO2 finite-difference scheme for the spatial resolution. Also, we have implemented the subcell fix resolution detailed in Min (2010), which modifies the ENO2 scheme near the interface in order to avoid artificial displacement of the interface during the redistancing iterative process.

3.2 Bingham projection

According to the rheological law (4), the plastic part $\boldsymbol{S}$ of the total stress tensor is simply given by $\boldsymbol{S} = \boldsymbol{D}(\boldsymbol{u})/|\boldsymbol{D}(\boldsymbol{u})|$, which is not well defined in the rigid zone, *i.e.* where the strain-rate tensor vanishes. In this case, the constraint $|\boldsymbol{S}| \leq 1$ should be added. A convenient way to define $\boldsymbol{S}$ is to use the formalism introduced in Chupin & Dubois (2016) (see also Chalayer *et al.*, 2018), that is

$$\boldsymbol{S} = P(\boldsymbol{S} + r\kappa(\phi)\boldsymbol{D}(\boldsymbol{u})), \quad \text{for any } r > 0, \tag{16}$$

where P is a projection operator which is explicitly defined by

$$P(\boldsymbol{L}) = \begin{cases} \frac{\boldsymbol{L}}{|\boldsymbol{L}|} & \text{if } |\boldsymbol{L}| > 1, \\ \boldsymbol{L} & \text{if } |\boldsymbol{L}| \leq 1, \end{cases}$$

for any traceless symmetric tensor $\boldsymbol{L}$. Note that the boundary condition (9) can be written similarly

$$\boldsymbol{T}_t = -\eta_{\mathrm{b}}\boldsymbol{u}_t - \kappa_{\mathrm{b}}(\phi)\boldsymbol{s}_t \quad \text{with} \quad \boldsymbol{s}_t = P_b(\boldsymbol{s}_t + r\kappa_{\mathrm{b}}(\phi)\boldsymbol{u}_t), \quad \text{for any } r > 0, \tag{17}$$

where $P_b(\boldsymbol{v}) = \begin{cases} \boldsymbol{v}/|\boldsymbol{v}| & \text{if } |\boldsymbol{v}| > 1, \\ \boldsymbol{v} & \text{if } |\boldsymbol{v}| \leq 1, \end{cases}$ for any vector $\boldsymbol{v}$. The complete system of equations is then formed by (13)-(15) supplemented with (16)-(17).

3.3 Chorin-Temam algorithm

Let $\delta t > 0$ be the time step. Assuming that the approximations $(\boldsymbol{u}^n, \phi^n, p^n, \boldsymbol{S}^n, \boldsymbol{s}_t^n)$ of $(\boldsymbol{u}, \phi, p, \boldsymbol{S}, \boldsymbol{s}_t)$ at discrete time $t_n = n\delta t$ are known, ϕ^{n+1} is computed as described in section 3.1. Note that $\boldsymbol{u}^n$, which is a solenoidal velocity field, is used to advect ϕ^n and then compute ϕ^{n+1}. We set: $\rho^{n+1} = \rho(\phi^{n+1})$, $\eta^{n+1} = \eta(\phi^{n+1})$, $\kappa^{n+1} = \kappa(\phi^{n+1})$, $\kappa_{\rm b}^{n+1} = \kappa_{\rm b}(\phi^{n+1})$ and $\eta_{\rm b}^{n+1} = \eta_{\rm b}(\phi^{n+1})$. The momentum equation is discretised with a second-order fractional time stepping scheme inspired from the pioneering Chorin-Temam algorithm (Chorin, 1968; Temam, 1969). This approach allows to decouple velocity and pressure in a step predicting a non-solenoidal velocity field followed by an update of the pressure used to project the estimated velocity onto the space of divergence-free velocity field. Following Chupin & Dubois (2016) and Chalayer *et al.* (2018), the prediction step reads

$$
\begin{aligned}
&\rho^{n+1}\left(\frac{3\tilde{\boldsymbol{u}}^{n+1} - 4\boldsymbol{u}^n + \boldsymbol{u}^{n-1}}{2\delta t} + 2\,\mathrm{div}\,(\boldsymbol{u}^n \otimes \boldsymbol{u}^n) - \mathrm{div}\,(\boldsymbol{u}^{n-1} \otimes \boldsymbol{u}^{n-1})\right) \\
&\qquad\qquad + \boldsymbol{\nabla} p^n = -\rho^{n+1} g \boldsymbol{e}_2 + \mathrm{div}\left(2\eta^{n+1}\boldsymbol{D}(\tilde{\boldsymbol{u}}^{n+1}) + \kappa^{n+1}\boldsymbol{S}^{n+1}\right) \\
&\boldsymbol{S}^{n+1} = P\big(\boldsymbol{S}^{n+1} + r\kappa^{n+1}\boldsymbol{D}(\tilde{\boldsymbol{u}}^{n+1}) + \theta(\boldsymbol{S}^n - \boldsymbol{S}^{n+1})\big), \quad \text{for any } r > 0,\ \theta \in (0,1), \\
&u_n = 0,\ \partial_n \boldsymbol{u}_t = 0, \text{ on } \partial\Omega_{\rm a}, \\
&\boldsymbol{T}_t^{n+1} = -\eta_{\rm b}^{n+1}\tilde{\boldsymbol{u}}_{\boldsymbol{t}}^{n+1} - \kappa_{\rm b}^{n+1}\boldsymbol{s}_t^{n+1}, \text{ on } \partial\Omega_{\rm w}, \\
&\boldsymbol{s}_t^{n+1} = P_b\big(\boldsymbol{s}_t^{n+1} + r_{\rm b}\kappa_{\rm b}^{n+1}\tilde{\boldsymbol{u}}_t^{n+1} + \theta(\boldsymbol{s}_t^n - \boldsymbol{s}_t^{n+1})\big), \quad \text{for any } r_{\rm b} > 0, \text{ on } \partial\Omega_{\rm w}.
\end{aligned}
\tag{18}
$$

Then, the projection step reads

$$
\begin{aligned}
&\rho^{n+1}\left(\frac{3(\boldsymbol{u}^{n+1} - \tilde{\boldsymbol{u}}^{n+1})}{2\delta t}\right) + \boldsymbol{\nabla}(p^{n+1} - p^n) = 0, \\
&\mathrm{div}\,\boldsymbol{u}^{n+1} = 0, \qquad (\boldsymbol{u}^{n+1} - \tilde{\boldsymbol{u}}^{n+1}) \cdot \boldsymbol{n} = 0 \text{ on } \partial\Omega
\end{aligned}
\tag{19}
$$

In (18), $(\tilde{\boldsymbol{u}}^{n+1}, \boldsymbol{S}^{n+1}, \boldsymbol{s}_t^{n+1})$ are nonlinearly coupled. Due to the non-differentiability of the viscoplastic rheology, a Newton algorithm can not be directly applied. Therefore, we use a Picard fixed point procedure to solve (18). The pseudo-relaxation terms depending on the parameter θ added in the projectors P and P_b allows for a geometric convergence with common ratio $(1-\theta)$ of the fixed point iterations; see Chupin & Dubois (2016) and Chalayer *et al.* (2018) for details. The projection step (19) consists essentially in solving a variable coefficients elliptic equation for p^{n+1} followed by a correction applied to the non solenoidal velocity $\tilde{\boldsymbol{u}}^{n+1}$ in order to obtain $\boldsymbol{u}^{n+1}$, which is divergence-free (up to the computer accuracy).

3.4 Numerical implementation

The aim of this paper being to numerically simulate, with a bi-dimensional model, the collapse of columns of granular matter in a rectangular channel, $\Omega = (0, \mathcal{L}) \times (0, \mathcal{H})$ will be used as computational domain. The initial granular column is defined by its length L_c and height H_c as it can be seen on figure 1 representing the configuration before release.

The computational domain is discretised in $\frac{\mathcal{L}n}{\mathcal{H}} \times n$ cartesian mesh cells. Let us denote by $h = \frac{\mathcal{H}}{n}$ the mesh size. As in the classical MAC scheme for the incompressible Navier-Stokes equations (Harlow & Welch, 1965) the discrete velocity unknowns $\boldsymbol{u}_{ij}$ are located at the midpoint of cell edges. The discrete pressure p_{ij} and level-set function ϕ_{ij} are placed at the centre of the mesh cell K_{ij}. All components of the plastic tensor $\boldsymbol{S}$ are also discretised at the centre of the mesh cell. This choice is arbitrary but allows to update all tensor components, through the local projection (16), at the same mesh locations (Chupin & Dubois, 2016).

The implementation has been done in a F90/MPI code previously written for one phase Bingham flows and used for simulating flows in a lid-driven cavity at Reynolds number up to 200 000 and

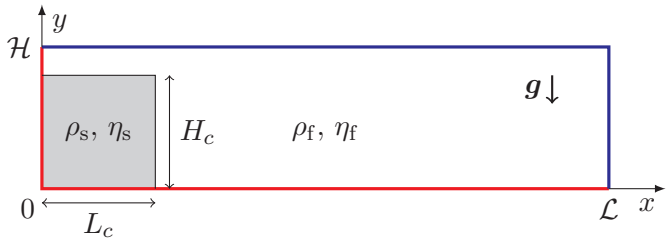

Figure 1: Configuration for the collapse of a granular column initially at rest. The blue part of the domain boundary corresponds to $\partial\Omega_a$ (free air) while the red one corresponds to $\partial\Omega_w$ (solid walls).

Bingham number equals to 100 (Chupin & Dubois, 2016). The PETSc library (Balay *et al.*, 2018*a*,*b*) is used to solve linear systems and to manage data on structured grids. The communications between the processes are explicitly written with MPI subroutines.

4 Results and comparisons with laboratory experiments

4.1 Collapse of a dry granular column with aspect ratio 0.7 over a rough surface

4.1.1 Experimental setup

We first consider an experiment in Mangeney *et al.* (2010) consisting of the collapse of a dry granular column (glass beads with diameter $d \approx 0.7$ mm ± 0.1 mm) in a 10 cm wide channel between plexiglass walls. The horizontal plane is 3 m long and is roughened by a layer of glass beads (with same diameter) glued on its surface. The granular medium is maintained in a reservoir of length $L_c = 20$ cm and height $H_c = 14$ cm, resulting in an aspect ratio $H_c/L_c = 0.7$, by the presence of a gate, which is opened at time $t = 0$ s. The particle density is $\rho_p = 2500\,\mathrm{kg\,m^{-3}}$ so that with a mass volume fraction of 0.62 the apparent flow density is $\rho_s = 0.62\rho_p = 1550\,\mathrm{kg\,m^{-3}}$.

4.1.2 Validation of the implementation of the DP-rheology

In order to validate the numerical implementation of the DP-rheology with constant viscosity as previously described, we first confront our results with the experiment and with those published in Ionescu *et al.* (2015). Indeed in Ionescu *et al.* (2015), numerical simulations corresponding to this experiment have been performed with a continuum model using the $\mu(I)$–rheology, reformulated in the framework of the Drucker-Prager rheology. Let us recall here this formulation. Following Jop & Pouliquen (2006), the $\mu(I)$–rheology can be written

$$\begin{cases} \boldsymbol{T'} = \mu(I)p\frac{\boldsymbol{D(u)}}{|\boldsymbol{D(u)}|} & \text{if } \boldsymbol{D}(\boldsymbol{u}) \neq 0, \\ |\boldsymbol{T'}| \leq \tan(\alpha)p & \text{if } \boldsymbol{D}(\boldsymbol{u}) = 0, \end{cases}$$

where $\mu(I) = \tan(\alpha) + \frac{\mu_\infty - \tan(\alpha)}{1+I_0/I}$, I_0 is a dimensionless number and $\mu_\infty \geq \tan(\alpha)$. The inertial number I is defined by

$$I = 2|\boldsymbol{D}(\boldsymbol{u})|d\sqrt{\frac{\rho_s}{p}}$$

with d the particle diameter of the granular material. By using the above definitions for I and $\mu(I)$, we can rewrite the expression of the tensor $\boldsymbol{T'}$ in regions where $\boldsymbol{D}(\boldsymbol{u}) \neq 0$ as

$$\boldsymbol{T'} = 2\eta(|\boldsymbol{D}(\boldsymbol{u})|, p)\boldsymbol{D}(\boldsymbol{u}) + \tan(\alpha)p\frac{\boldsymbol{D}(\boldsymbol{u})}{|\boldsymbol{D}(\boldsymbol{u})|}$$

where $\eta(|\boldsymbol{D}(\boldsymbol{u})|,p)=\frac{(\mu_\infty-\tan(\alpha))p}{2|\boldsymbol{D}(\boldsymbol{u})|+I_0\sqrt{p}/d\sqrt{\rho_s}}$. Instead of the above expression for $\boldsymbol{T'}$, we use a similar rheology but replace the viscosity $\eta(|\boldsymbol{D}(\boldsymbol{u})|,p)$ prescribed by the $\mu(I)$–rheology with a constant viscosity η_s in the present study (see (4)–(6)). Note that very little differences were found in Ionescu *et al.* (2015) between results obtained with constant and variable viscosity. Also, the authors estimated values for η_s in the range $[0.1,1]$Pa s by using the $\mu(I)$–rheology. We choose the value $\eta_s=0.5$ Pa s for the simulations presented in this section.

Let us highlight the major differences between our numerical implementation of the DP-rheology and the one used in Ionescu *et al.* (2015). In Ionescu *et al.* (2015), the presence of the ambiant gaz (air) is not accounted for and equations of motions are only solved in the viscoplastic fluid domain, *i.e* containing the granular material. In our study, both the granular and the ambient flow are modeled through a level-set formulation (see section 3). Another difference is the presence of the gate, which is not modeled in our numerical simulations, but is accounted for with a time shift of -0.03 s, which is half the lifting time of the gate. In order to compare our numerical results with those in Ionescu *et al.* (2015), the same rheological parameters are used and the reader is referred to Ionescu *et al.* (2015) for explanations of the chosen values. The friction coefficient of the glass beads on the plexiglass wall at the back of the channel is $\kappa_b=\tan(10.5^\circ)=0.18$ while $\kappa_b=\tan(25.5^\circ)=0.48$ is used on the rough horizontal plane. The static friction coefficient in the yield (6) and (7) is $\tan(25.5^\circ)=0.48$.

In figure 2, the granular mass at different times during its collapse is plotted and compared with the profile of the experiment and of the numerical results presented in Ionescu *et al.* (2015). Note that here, the numerical simulation is performed by using 256 mesh points in the vertical direction, which corresponds to a mesh size $h=0.4/256=0.78125$ mm similar to the size of the glass beads used in the experiment; in Ionescu *et al.* (2015), the resolution was coarser with the mesh size in the interval $[3.3,10]$ mm. We observe on figure 2 that the height of the granular column on the back wall of the reservoir is maintained at its initial value during the whole collapse as in the experiment while in Ionescu *et al.* (2015) the height of the final (stationary) state is underestimated by nearly 10%. The plateau, corresponding to the left upper part of the granular mass (and touching the back plexiglass wall), found in the experiment is very well captured by our numerical simulation. In both simulations, the fronts of the granular masses, corresponding to the most advanced part of the sliding material located on the horizontal plate, are slightly ahead of the experimental front during the first half period of the collapse, that is for $t\leq 0.42$ s. This may be explained by the presence of the gate, which is not properly accounted for in the numerical methods so that small differences on the dynamics are observed at the beginning of the collapse process, namely the acceleration phase.

At the final stage, $t=1.06$ s, the profile of the granular mass is noticeably well predicted by our simulation with the DP-rheology. Note, however, that the experimental runout distance is underestimated by about 7.5%. We will show below that the value of the viscosity η_s has an influence on the runout distance, which can be more accurately predicted with smaller values of η_s. Note that the simulation in Ionescu *et al.* (2015) found a runout distance overestimated by only 1.4% but the height of the mass at the back wall 10% smaller was obtained though in the experiment the material in this zone remained static. The slope of the deposit as well as the overall distribution of the granular mass is more accurate in our simulation.

It is well known (Della Rocca & Blanquart, 2014) that the level-set method, especially the reinitialisation procedure, which is mandatory so that the level-set function remains signed distance, cannot predict the angle of the interface with walls for contact line problems. However, as shown on figure 2, the front of the deposit at $t=1.06$ s is found to be almost as thin as the experimental one. Note that, according to Della Rocca & Blanquart (2014), we have adapted the high order ENO and WENO schemes at the walls by reducing their order of accuracy when mesh points are close to the boundaries so that no extrapolations at exterior *ghost* points are used. This allowed to stabilise the level-set solver. We infer that the implementation of the Coulomb friction law (9)–(11) at the boundaries is essential in order to obtain a so thin interface close to the ground level. Indeed,

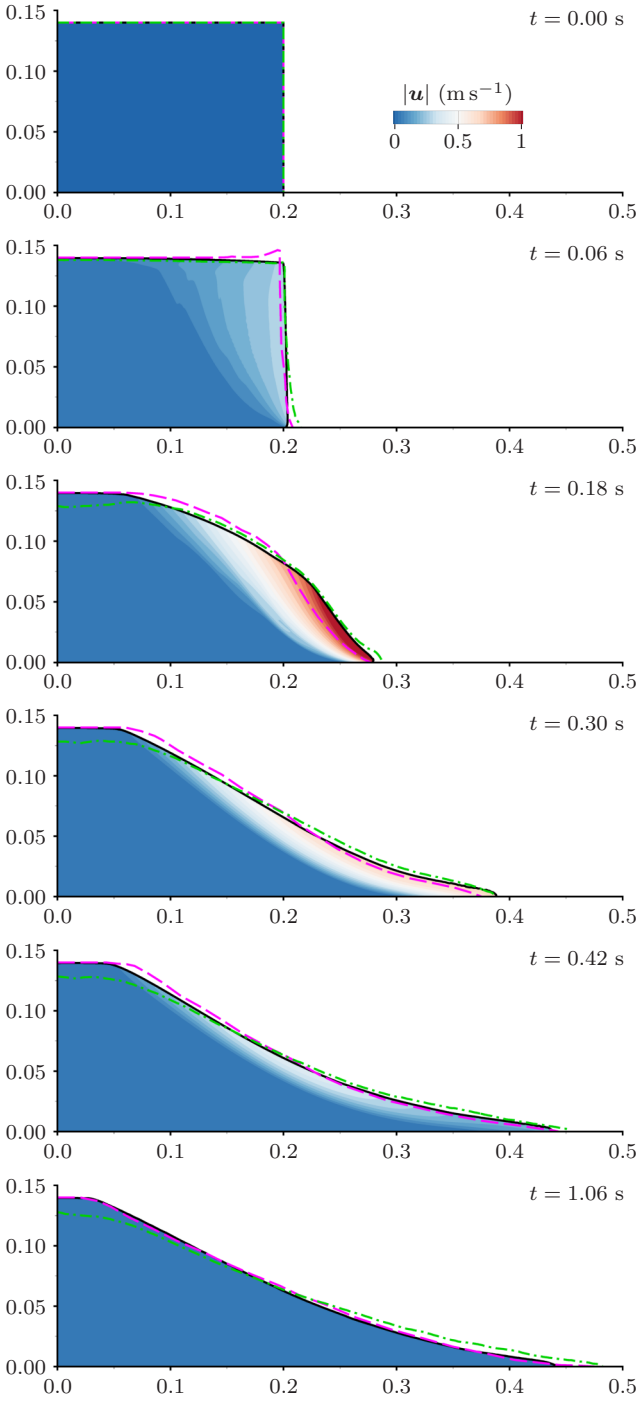

Figure 2: Comparison between numerical and experimental (pink dashed curve) results of the collapse of a granular mass. The colour scale corresponds to the velocity Euclidean norm $|\boldsymbol{u}|$ (in m s^{-1}) computed by using the DP-rheology. The black solid curve corresponds to the DP-rheology model while the green dot-dashed one () is from Ionescu *et al.* (2015). The numerical resolution is $h = 0.78125 \times 10^{-3}$ m and the computational domain is $\Omega = (0, 0.8) \times (0, 0.2)$.

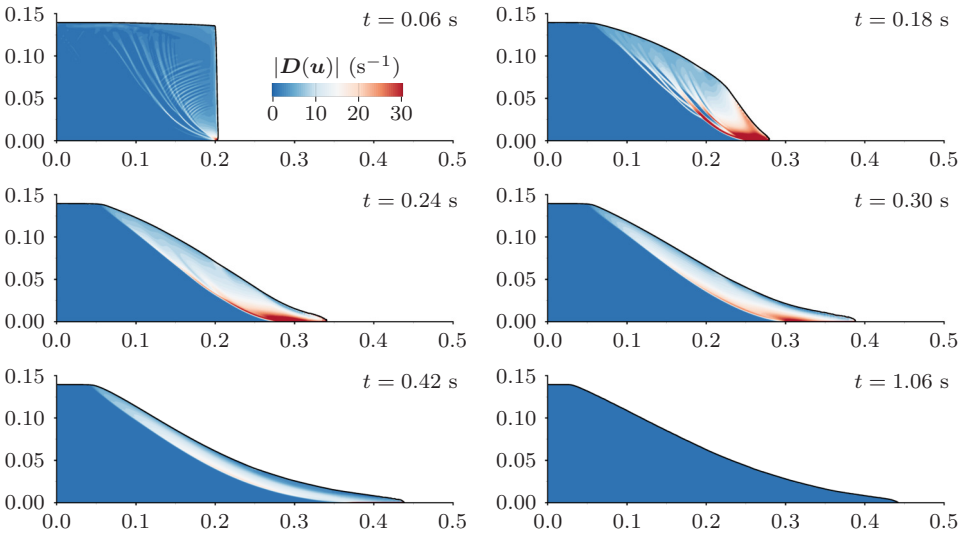

Figure 3: Strain rate $|\boldsymbol{D}(\boldsymbol{u})|$ (in s^{-1}) at different times during the granular mass collapse simulated with the DP-rheology. The numerical resolution is $h = 0.78125 \times 10^{-3}$ m and the computational domain is $\Omega = (0, 0.8) \times (0, 0.2)$.

the frontal part of the experimental deposit at the final time has only one glass bead depth, that is 0.7 mm±0.1 mm, over a horizontal distance of 1.5 cm ($\approx$ 20 glass beads). As shown on figure 2, the result from Ionescu *et al.* (2015), where a different numerical treatment of the interface is used, overestimates the thickness of the deposit at the front and on a large area, that is for $x \geq 0.25$, resulting in a less accurate estimate of the slope of the deposit. As in Ionescu *et al.* (2015), the volume loss of the granular mass during the numerical simulation is below 0.84%. Also shown on figure 2 is the Euclidean norm of the velocity field inside the granular mass during the collapse. This provides information on the flow dynamics. As it has been observed in experiments and in other numerical simulations (Lacaze *et al.*, 2008; Lacaze & Kerswell, 2009; Crosta *et al.*, 2009; Lagrée *et al.*, 2011; Ionescu *et al.*, 2015), two zones in the granular mass can be identified during the collapse: a static one, corresponding to the basal deposit which is growing with time and which has no motion, and a mobile one where glass beads are moving. The deposit shown in blue represents a large part of the granular mass. The motion occurs in a narrow sublayer, underneath the surface down to the ground and behind the front, and in the early stage of the collapse, that is for time $t \in [0, 0.42]$ s. At $t = 0.42$ s, the front has reached the maximum runout distance. During the second half of the experiment, *i.e.* for $t \geq 0.42$ s, the deposit represents an increasing part of the whole granular mass until a stationary state is reached for t near 1.06 s.

Contours of the basal deposit and of the moving layer are also well defined by using the strain rate $|\boldsymbol{D}(\boldsymbol{u})|$ as discriminant quantity. Indeed, in viscoplastic fluids plugs and dead zones correspond to areas where the strain rate vanishes; both strain rate and velocity vanish in dead zones. On the other hand, non-zero values of the strain rate indicate motion with deformations. This is clearly visible on figure 3, which shows most intense shear along the bottom wall at the flow head.

On figure 4 representing the pressure, spatial oscillations, similar to characteristic lines for hyperbolic problems, develop as soon as motion starts ($t = 0.06$ s) and are persistent during the whole collapse. Such oscillations have also been identified by Martin *et al.* (2017) and seem to be inherent to pressure dependent rheology, certainly related to the "ill–posedness" nature of the mathematical model. More precisely, it is well known that the DP-model is ill-posed (Schaeffer, 1987; Schaeffer & Pitman, 1988) and that some oscillations are likely to appear. Mathematically ill-posed problems suffer from unbounded growth of short wavelength perturbations, which necessarily lead to grid dependent numerical results that do not converge as the spatial resolution is enhanced.

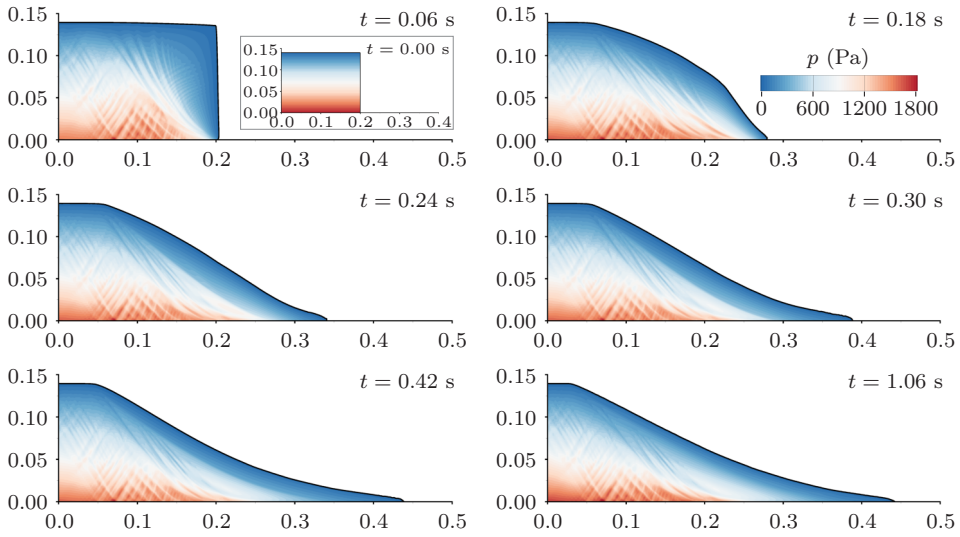

Figure 4: Pressure p (in Pa) at different times of the granular collapse simulated with the DP-rheology. The initial static state at $t = 0$ s is also shown. Note that a different scale is used for the initial pressure for which maximum value is about 2 129 Pa. The numerical resolution is $h = 0.78125 \times 10^{-3}$ m and the computational domain is $\Omega = (0, 0.8) \times (0, 0.2)$.

In practice, a more complex rheology, the $\mu(I)$-rheology, is well-posed for intermediate values of the inertial numbers I, but it remains ill-posed for both high and low inertial numbers (Barker *et al.*, 2015). Note that recently, in Barker & Gray (2017), changes to the functional form of the $\mu(I)$ curve have been considered in order to maximise the range of well-posed inertial numbers. Barker & Gray (2017) shows that when the inertial number is low there exists curves for which the equations are guaranteed to be well-posed. However, despite the presence of pressure oscillations, the granular mass spreading is well predicted by the DP-model, and the shape of the granular mass as well as its contours are accurately computed. By refining the mesh, we did not observe amplifications of these oscillations. Moveover, pressure remains bounded and for all simulations $\max_{\Omega_s} p \leq \rho_s g H_c \approx 2129$ Pa, where Ω_s is the part of the computational domain filled by glass beads ($\rho = \rho_s$).

4.1.3 Numerical convergence

In order to investigate the sensitivity of the numerical results with respect to the mesh resolution, we performed numerical simulations with $n = 64$, 128 and 256. The time step, adjusted in order to ensure CFL stability condition for the finer mesh, is equal to $\delta t = 10^{-4}$ s. The mesh size dependency is analysed by focusing on the shape of the interface between the granular material and ambiant air at $t = 1.06$ s (see figure 5), that is when the stationary state of the deposit is reached, and on the dynamics of the collapse by plotting the time evolution of the distance of the front at the bottom level from the back wall (see figure 6). It can be clearly observed on figure 5 that the deposit of the granular mass depends weakly on the resolution: results with different mesh sizes are very close to each other. The most important difference is found by comparing the computed runout distances: the value predicted with $n = 64$ is smaller than values obtained with $n = 128$ and $n = 256$, which are close to each other, indicating numerical convergence. As it was mentioned in the previous section, the front of the simulated deposit is slightly thicker than what is observed in experiment. However, it is much thinner than what could be expected considering the fact that the level-set method is used to compute the interface. Indeed, the latter is known to have inherent difficulties to accurately compute the angle of the interface with walls for contact line problems such as the one considered in this paper. The use of the Coulomb friction law at

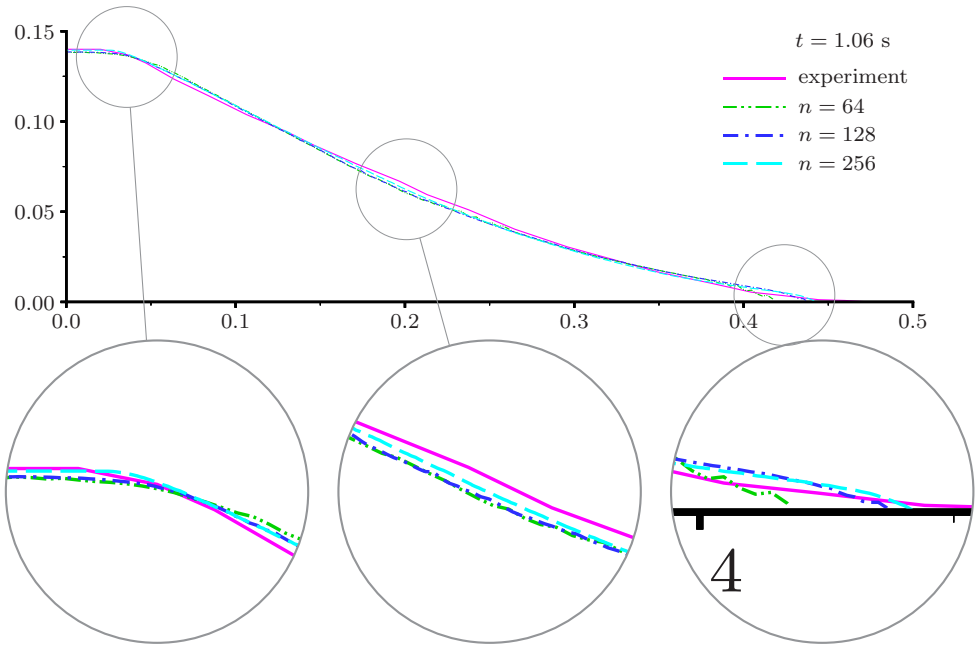

Figure 5: Profiles of the granular mass at the stationary state obtained with the DP-rheology with different mesh resolutions: $n = 64$ ($h = 3.125 \times 10^{-3} m$), $n = 128$ ($h = 1.5625 \times 10^{-3}$ m) and $n = 256$ ($h = 7.8125 \times 10^{-4}$ m). Note that the size of the finer mesh is of the order of the particle diameter (0.7 ± 0.1 mm).

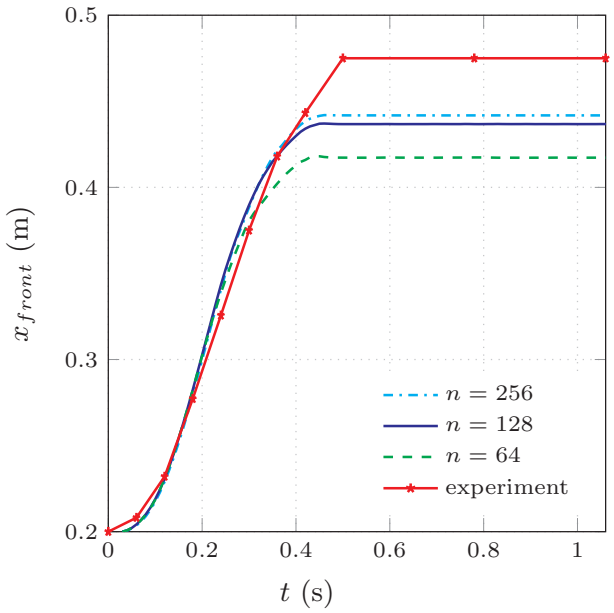

Figure 6: Plot of the front position as a function of time during the spreading of the granular mass. The front stops at $t = 0.5$ s while the upper part of the basal deposit still moves up to $t = 1.06$ s where a stationary state is reached. Results from simulations using different mesh sizes are shown and compared to the experimental measurement. Simulations in the computational domain $\Omega = (0, 0.8) \times (0, 0.2)$ are performed with the DP-rheology.

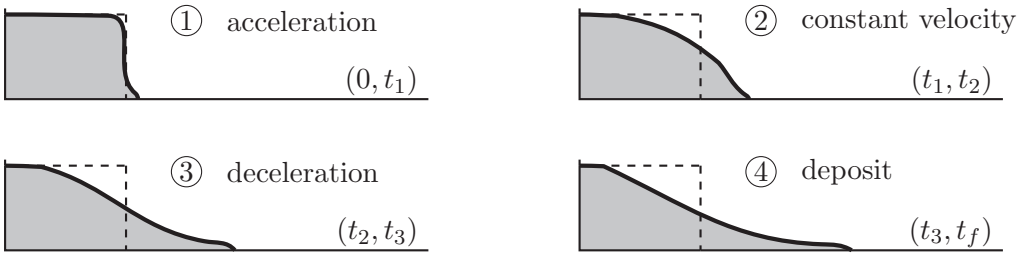

Figure 7: The four stages of the granular mass collapse.

the bottom boundary is compulsory in order to obtain a good approximation of the interface at the front end of the deposit. The simulation on the finer mesh was performed by using 16 MPI processes during 9 days (waiting time). Note that the mesh size for $n = 256$ is $h = 0.78125 \times 10^{-3}$ m, which corresponds to the diameter of the glass beads ($d = 0.7 \pm 0.1$ mm).

A good agreement between simulated and experimental results is also obtained for the prediction of the mass spreading as shown on figure 6. Only the last measured point ($x = 0.4750$ m) is missed by the numerical simulations, which stop at 0.442 m for the finest resolution. Note that on the last 1.5 centimeters, corresponding to 20 glass beads, the experimental deposit has a thickness of the order of 0.8 mm, which means than the last visible particle locates at $x = 0.4750$ m. For a numerical method solving a continuous fluid model with interface tracking, being able to capture a front end of one mesh size high extended on 20 mesh sizes seems to be unattainable. We will see in the next section that reducing the value of the viscosity η_s improves the approximation of the runout distance. Despite this reasonably small discrepancy, the overall time history of the front is accurately captured. Indeed, as in the experiment, four time phases are clearly identified: the time interval $(0, t_f)$, where t_f is the time where steady state is reached, can be split into four sub-intervals with bounds denoted by t_1, t_2, t_3, t_f (see figure 7). During the first stage, for $t \in (0, t_1)$ s, acceleration occurs once the gate is lifted, then for $t \in (t_1, t_2)$ s the front moves forward at a constant speed. In the following phase $t \in (t_2, t_3)$ s the flow decelerates and, finally, over a longer time interval $t \in [t_3, t_f]$ s the front has reached the runout distance and does not advance anymore, while the upper surface of the basal deposit still moves upwards very slowly until it reaches the surface at $t = t_f = 1.06$ s. From figure 6, we may infer values of the bounds t_i, $i = 1, 2, 3$: $t_1 \approx 0.1$ s, $t_2 \approx 0.35$ s and $t_3 \approx 0.45$ s. Note that during the last time interval, $t \in (0.45, 1.06)$ s, which is more than half of the whole time interval of the simulation, the motion at the surface of the granular material is very slow while the front has already reached the runout distance of the granular collapse. During the constant propagation speed phase the front is found in the experiment to move at a speed equal to 0.775 m s^{-1} while the numerical simulations predict a faster displacement ≈ 0.952 m s^{-1}. This was also observed in Ionescu *et al.* (2015).

An important parameter in the numerical algorithm is the pseudo–relaxation coefficient θ added in the Bingham projection in order to ensure geometrical convergence of the Picard's algorithm used to solve the coupling in (18) (see also Chupin & Dubois, 2016; Chalayer *et al.*, 2018). This parameter must be chosen sufficiently small in order to ensure that the plastic part of the stress tensor is well resolved. The theory suggests that θ should be of the order of the time step δt (see Chupin & Dubois, 2016; Chalayer *et al.*, 2018) ensuring the time scheme to be first order accurate. In practice, we found that using $\theta = 10\,\delta t$ as value for this parameter provided accurate predictions of the slump dynamics. This value is optimal in the sense that it reduces the computational cost and ensures accurate results.

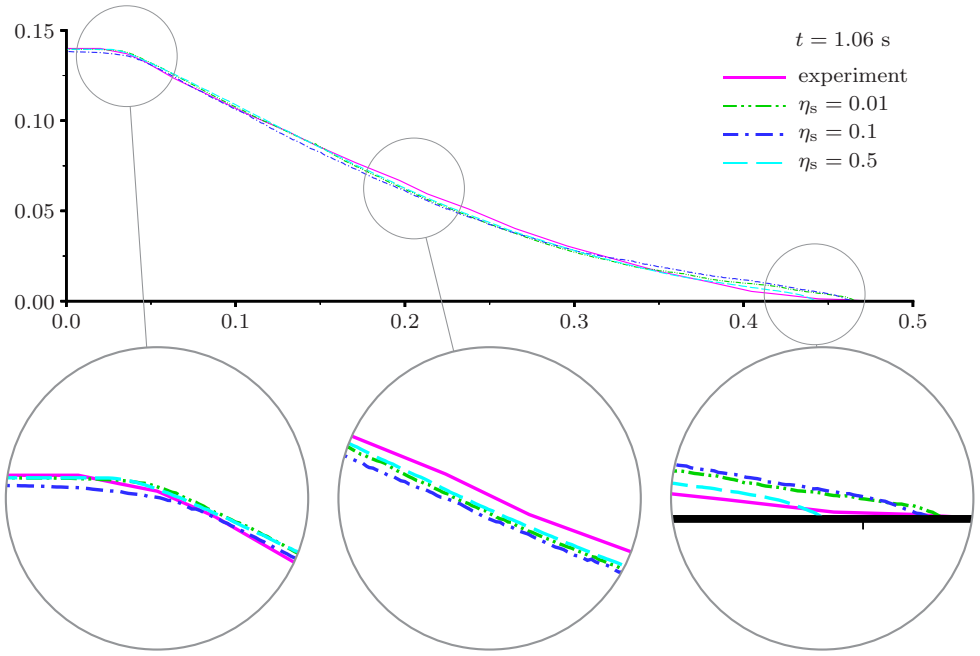

Figure 8: Profile of the granular deposit at $t = 1.06$ s obtained for various values of the viscosity η_s in the DP-rheology. The resolution corresponds to the finer mesh with $h = 0.78125 \times 10^{-3}$ m and the computational domain is $\Omega = (0, 0.8) \times (0, 0.2)$.

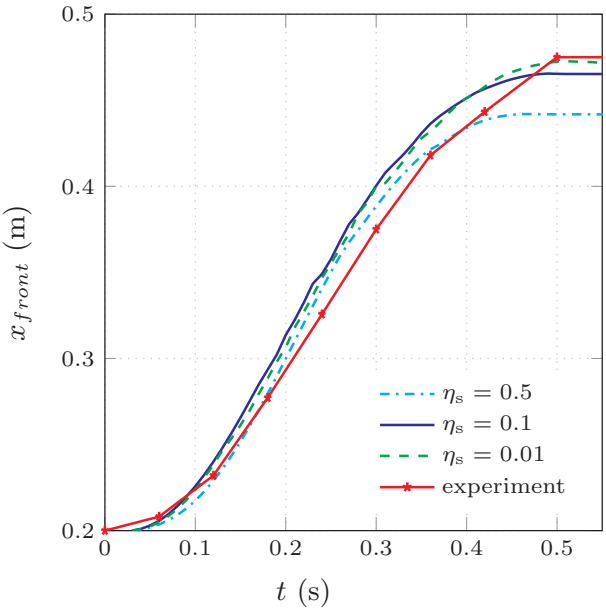

Figure 9: Plot of the front position as a function of time during the spreading of the granular mass. The front stops at $t = 0.5$ s. Results from simulations performed with the DP-rheology and using different values of the viscosity η_s are shown and compared to the experimental measurement. The computational domain is $\Omega = (0, 0.8) \times (0, 0.2)$ and the mesh size is $h = 0.78125 \times 10^{-3}$ m.

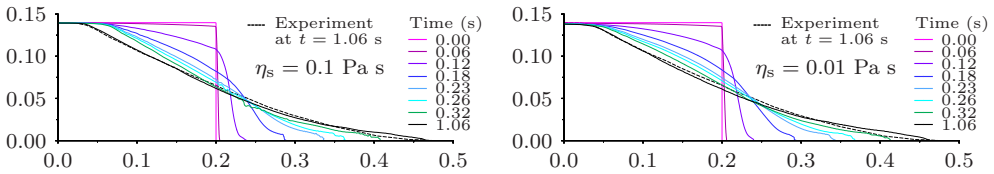

Figure 10: Time evolution of the profile of the granular mass during its collapse obtained with the DP-rheology and simulated with viscosity $\eta_s = 0.1$ Pa s (left) and $\eta_s = 0.01$ Pa s (right). The computational domain is $\Omega = (0, 0.8) \times (0, 0.2)$ and the mesh size is $h = 0.78125 \times 10^{-3}$ m.

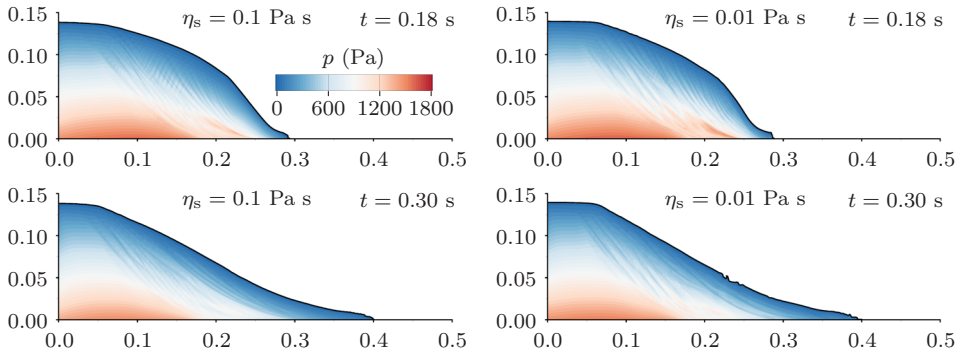

Figure 11: Comparison of dynamic pressure p (in Pa) with respect to different viscosity values η_s (in Pa s). The granular collapse is simulated with the DP-rheology. The numerical resolution is $h = 0.78125 \times 10^{-3}$ m and the computational domain is $\Omega = (0, 0.8) \times (0, 0.2)$.

4.1.4 Influence of the value of the viscosity η_s on the numerical results

We conclude the analysis of the results obtained with the DP-model for the 0.7 aspect ratio column by estimating the influence of the viscosity coefficient η_s. As it was mentioned in section 4.1.2, all previously discussed simulations were conducted with the value 0.5 Pa s for η_s. This choice was made following the estimates provided in Ionescu *et al.* (2015). Using smaller values of η_s will attest the robustness of our code and of the implementation with a bi-projection scheme in the framework of level-set method of the DP-model. From a physical point of view, as the value of this granular viscosity is *a priori* not known, investigating the dependency of the results upon this parameter is relevant. In order to complete our study, we performed simulations with $\eta_s = 0.1$ Pa s and 0.01 Pa s. Note that in Ionescu *et al.* (2015), values of the viscosity for the DP-model, but with a different numerical implementation, in the range $[0.1, 10]$ Pa s have been used. The authors mentioned that, for computational issues, they were not able to take smaller values of η_s. Setting $\eta_s = 0.01$ Pa s with our parallel code did not induce any technical difficulty. The time step, for stability reason, was divided by two and the number of MPI processes was doubled in order to keep constant the computational costs. Figure 8 shows profiles of the granular mass at stationary state obtained with the considered values of the viscosity and compared with the experimental one. First of all, the overall distribution of the granular mass in the domain is weakly influenced by the value of the viscosity. The best result is obtained with $\eta_s = 0.01$ Pa s for which an almost perfect match with the experimental deposit is found. Indeed, the runout distance increases as η_s decreases and almost matches the experimental value. Figure 9 indicates a convergence with respect to the value of η_s. The height of the granular mass at the back wall is also well approximated: 0.1384 m, which is only 1.5% below the experimental value. All profiles are very similar and close to each other. The front of the granular mass propagates slightly faster for values of the viscosity smaller than 0.5 Pa s but the curves for $\eta_s = 0.1$ Pa s and 0.01 Pa s are close to each other up to $t = 0.3$ s

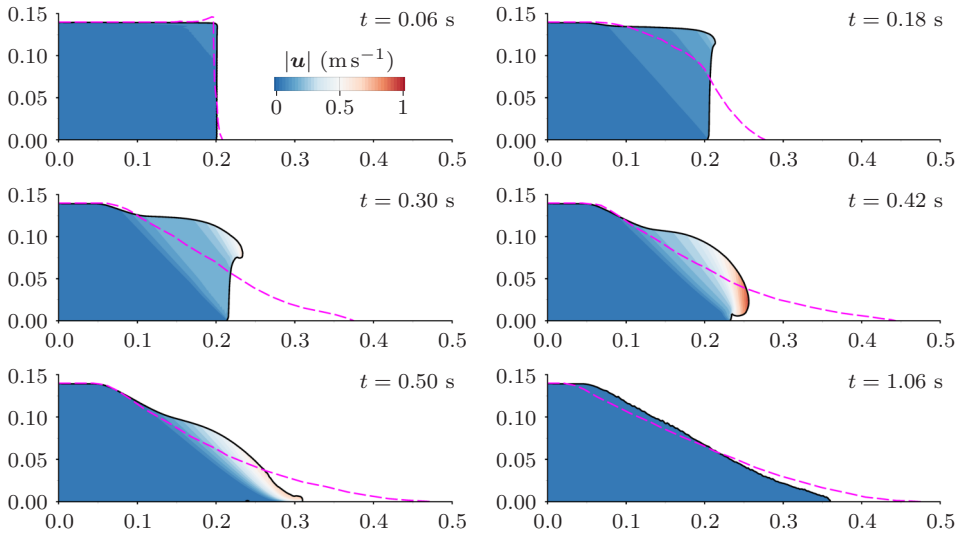

Figure 12: Comparison between numerical (black solid curve) and experimental (pink dashed curve) results of the collapse of a granular mass. The colour scale corresponds to the velocity Euclidean norm $|\boldsymbol{u}|$ (in m s^{-1}). The HP-rheology model is used. The numerical resolution is $h = 0.15625 \times 10^{-2}$ m and the computational domain is $\Omega = (0, 0.8) \times (0, 0.2)$.

(see figure 9). Figure 9 is completed by figure 10, which shows profiles at different times during the collapse obtained with $\eta_s = 0.1$ Pa s and $\eta_s = 0.01$ Pa s. Differences in the profiles occur in the aera $x \in [0.05, 0.1]$ m where the height of the granular flow is larger with $\eta_s = 0.01$ Pa s. As a consequence, the slopes of the profiles are steeper for $x \in [0.1, 0.2]$ m. The overall behaviour of the collapse is well captured and values of the viscosity have minor effects on the flow dynamics.

On figure 11, we observe that the dynamic pressure is affected by the value of the viscosity. Namely, in the area corresponding to the basal deposit, the pressure has less small-scale oscillations for the simulations performed with the values $\eta_s = 0.1$ and 0.01 Pa s than with $\eta_s = 0.5$ Pa s. These oscillations are persistent and still visible but mainly in the sublayer where the flow motion occurs. These results are counter-intuitive as the DP yield stress, *i.e.* without viscosity, yields itself to an ill–posed model.

As a summary, the dependency of the numerical results upon the value of η_s is very weak, thus attesting the robustness of both the DP-rheology and the numerical implementation used in this paper.

4.1.5 The HP-rheology

One of the objectives of this work is to compare the two usual pressure chosen as a threshold in the viscoplastic rheology defined in (4). In the DP-model, $\kappa = \tan(\alpha)p$ is used as yield stress where p is the total pressure of the flow whereas in the HP-model the choice of the hydrostatic pressure $p_{\text{hyd}}(x, y) = \displaystyle\int_y^{\text{top}} \rho(x, z)\, g\, dz$ in the threshold $\kappa = \tan(\alpha)p_{\text{hyd}}$ is made, where "top" is the heigth of the granular mass. The motivation for introducing the HP-model is that it has been proven in Chupin & Mathé (2017) to be well-posed, unlike the DP-rheology. However, from the best of our knowledge, the HP-model has never been used to perform simulations of the gravitational collapse of a granular column. We hereafter investigate the applicability of the HP-rheology in this context. The spatial resolution and the computational domain used are respectively $n = 256$ ($h = 0.78125 \times 10^{-3}$ mm) and $\Omega = (0, 0.8) \times (0, 0.2)$. The viscosity η_s was set to 0.5 Pa s. As shown on figure 12, the prediction, provided by the HP-rheology, of the shape of the granular

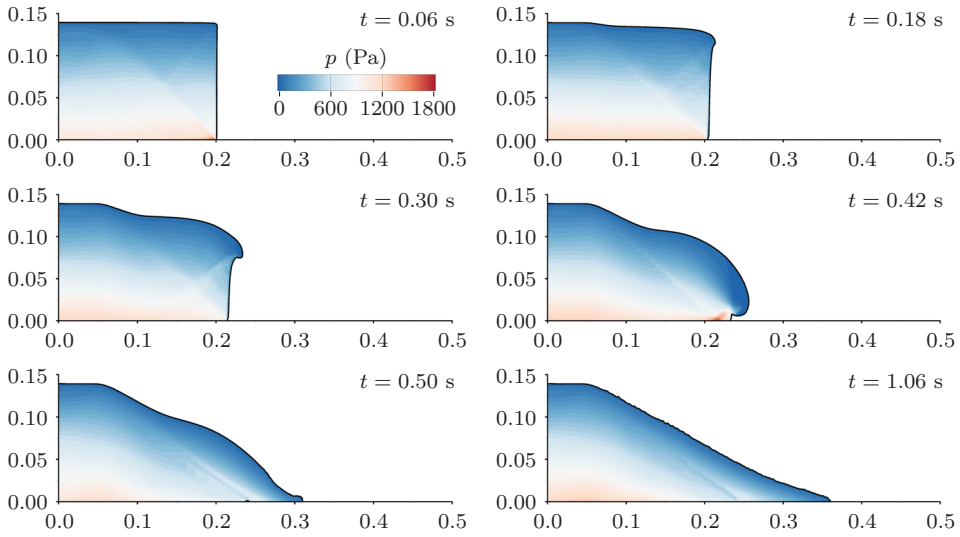

Figure 13: Pressure p (in Pa) at different times during the granular mass collapse computed with the HP-rheology. The numerical resolution is $h = 0.15625 \times 10^{-2}$ m and the computational domain is $\Omega = (0, 0.8) \times (0, 0.2)$.

deposit at steady state is acceptable: the height at the back wall has the correct value, the slope of the deposit downstream the left plateau is slightly larger than the expected one and, the runout distance is underestimated by 24% compared to the experimental value. However, the HP-model fails to reproduce the correct dynamics. After the acceleration phase, *i.e.* at $t \geq 0.18$ s, a small bump appears at the right upper corner of the granular mass. It further develops into a growing, non physically relevant protuberance for $t \in [0.3, 0.42]$ s. The strength of the threshold, being vertically stratified by definition, is far too strong at the ground level and as a result the right margin of the granular column moves very slowly as a block and the interface with air remains vertical. Finally, a transition occurs for times in the interval $[0.42, 0.5]$ s characterised by the fall of the nose-like bump on the horizontal surface. Note that the phase near $t = 0.42$ s is critical and difficult to capture with an interface tracking method as the slump moves down and touches the ground. This shows the robustness of our implementation of the level set method in the context of viscoplastic dambreak problems. Further in time, the front moves forward very slowly and the stationary stage is reached for $t \approx 1.06$ s as for the experiment and the DP-model simulations. Note that as in the simulations with the DP-rheology, static and moving zones can be identified from the values taken by the velocity and/or strain-rate norms (figure 13 and 14). Unlike the DP-model, the pressure as well as the strain rate predicted by the HP-model are smooth and have no oscillations (see figures 13 and 14). This is due to the fact that the model based on the HP-rheology is well-posed and provides smooth solutions. Note however, that the order of magnitude of these quantities are similar for both models. As a summary, the HP-model produces an acceptable steady state (*i.e.* deposit) but fails to reproduce the dynamics of the granular slump. Moreover, non physical solutions are observed during the transient phase. As it was previously done with the DP-model, numerical simulations with values of the viscosity set to $\eta_s = 0.1$ Pa s and $\eta_s = 0.01$ Pa s were performed. It can be seen on figure 15 that the value of the viscosity has an impact on the runout distance: a smaller value of η_s increases the maximum distance reached by the HP-model simulations. However, the transient profiles are also non physically relevant and the flow dynamics is weakly influenced by the value of the viscosity and is therefore governed by the apparent viscosity due to the yield stress.

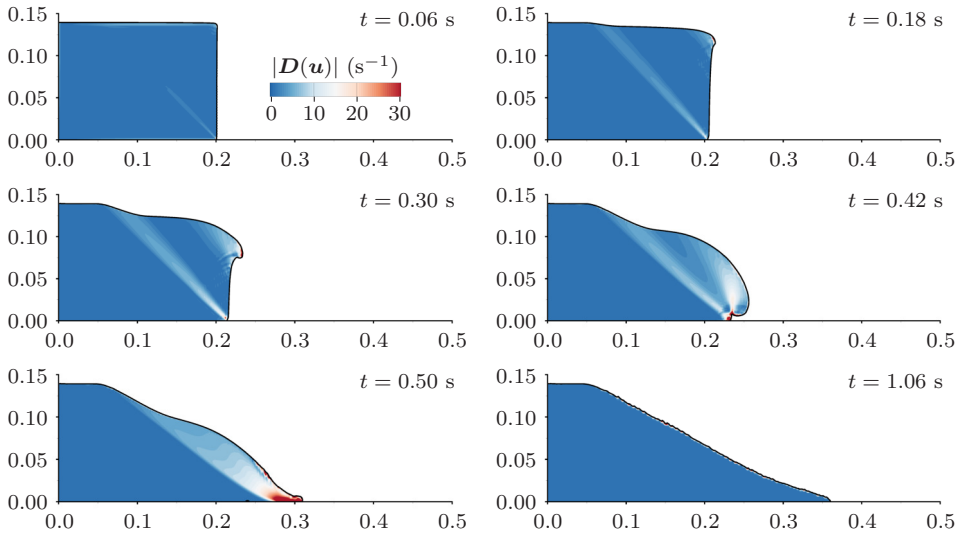

Figure 14: Strain rate $|\boldsymbol{D}(\boldsymbol{u})|$ (in s^{-1}) at different times during the granular mass collapse computed with the HP-rheology. The numerical resolution is $h = 0.15625 \times 10^{-2}$ m and the computational domain is $\Omega = (0, 0.8) \times (0, 0.2)$.

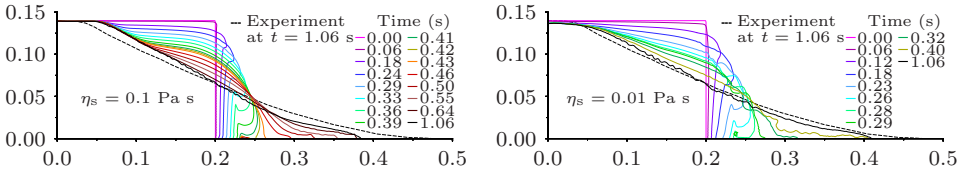

Figure 15: Time evolution of the profile of the granular mass during the collapse obtained with the HP-rheology and simulated with viscosity $\eta_s = 0.1$ Pa s (left) and $\eta_s = 0.01$ Pa s (right). The numerical resolution is $h = 0.15625 \times 10^{-2}$ m and the computational domain is $\Omega = (0, 0.8) \times (0, 0.2)$.

4.2 Collapse of a dry granular column with aspect ratio 2 over a smooth surface

4.2.1 Experimental setup

Note that from the best of our knowledge, the results presented below are the first ones comparing numerical simulations with an experiment carried out by Roche *et al.* (2010) with an initial column of width $L_c = 20$ cm and height $H_c = 40$ cm. Moreover, due to the fact that the aspect ratio of the column is larger than unity, depth-averaged models can not be used. The glass beads used in this case are ten times finer than the ones used in the previous experiment and have a (mean) diameter $d = 0.08$ mm. The reservoir $(0, L_c) \times (0, H_c)$ is connected with a channel with a smooth base, which is 10 cm wide and 3 m long, through a gate opened at $t = 0$ s. In our numerical simulations, the gate is not modelled and we assume that the whole granular column is released at $t = 0$ s. The particle density is $\rho_p = 2500\,\mathrm{kg\,m^{-3}}$, which leads to an apparent flow density $\rho_s = 1550\,\mathrm{kg\,m^{-3}}$ (a mass volume fraction of 0.62 is taken into account). The static (inner) friction coefficient for the considered glass beads is determined from 27°, which is equal to the material repose angle (Roche, 2012).

4.2.2 Influence of the basal friction angle

The friction angle of the glass beads on the plexiglass plates of the channel is estimated by considering, at increasing slope angles, onset of motion of a layer of beads covered by a solid metal

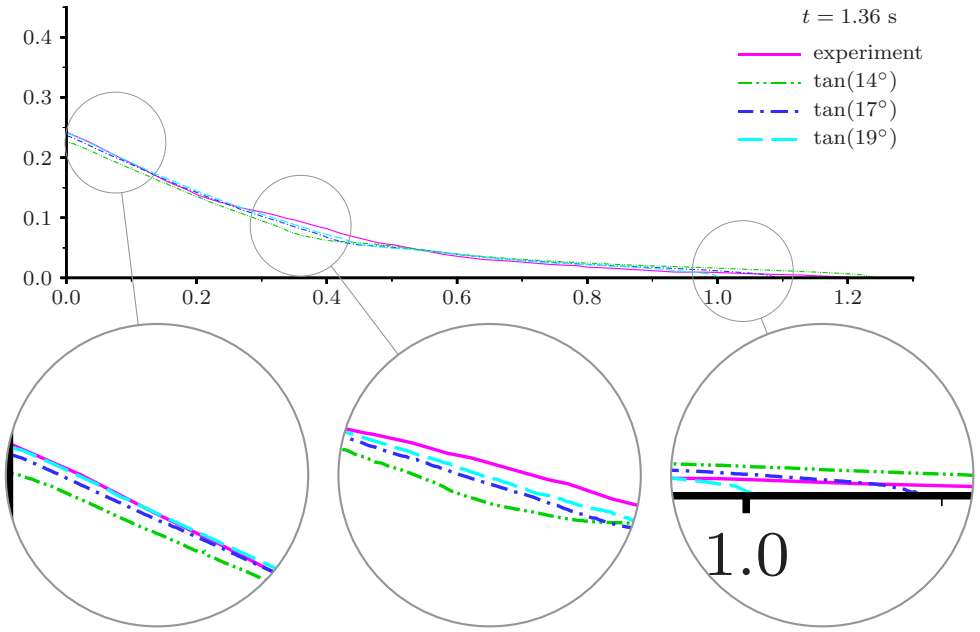

Figure 16: Profiles of the granular mass at the final time of the mass spreading obtained with the DP-rheology for the $(0, 0.2) \times (0, 0.4)$ initial column. Profiles obtained with different basal friction angles (14°, 17° and 19°) are shown and compared with the experimental result.

block. When the beads are free to roll, the block moves at an angle of $8° \pm 1°$. Note that with this technique, it is almost impossible to be sure that glass beads do not overlap and that the thickness of the basal layer remains equal to the particle diameter during the test. Furthermore, the apparent low friction angle is most certainly due to rolling of the particles. In contrast, when the layer of glass beads is glued to the block, the onset of motion of the block occurs at an angle of 19°, which is assumed to be close to the friction angle between the beads and the plates. Notice that this value was considered in Gueugneau *et al.* (2017). Unlike for the experiment at aspect ratio 0.7, we assume that the friction angles for all contact surfaces, namely both the vertical back wall and the bottom plate, have the same value, which is chosen close to 19° as stated above. In order to estimate the influence of the basal friction angle on the dynamics of the granular mass slump, we retained the three following representative values: 14°, 17° and 19°. On figure 16, we compare the mass profiles at the final time, namely $t = 1.36$ s, of the collapse of the granular column obtained with the DP-rheology, on a grid with 768×256 mesh points ($h = 0.46/256 \approx 1.8$ mm); the time step has to be set to $\delta t = 10^{-4}$ s in order to ensure numerical stability. Note that in this case the mesh size h is 22.5 times larger than the particle size. Using a mesh with two times more points will increase the amount of computational resources (CPU time and number of MPI processes) required but remain feasible. Nevertheless, using a mesh as fine as the glass beads as in section 2 is out of reach. Therefore, the choice of a grid with 768×256 mesh points is a good compromise between the amount of computational resources involved and the waiting time to get simulations done (8 days with 32 MPI processes).

Figure 16 shows that the values tan(17°) and tan(19°) for the basal friction coefficient give very similar approximations of the profile of the final deposit, *i.e.* at $t = 1.36$ s. For these coefficients, the runout distances are respectively underestimated by 9% and 17%. Close to the back wall, *i.e.* for $x \leq 0.3$ m, the numerical profile, obtained with tan(17°), is 2.5% below the experimental one while a perfect match is found with tan(19°). With the smallest angle 14°, the front stops at 1.205 m compared to 1.2 m for the experiment but the height of the granular mass on the interval $x \in [0, 0.35]$ m is underestimated by nearly 7%.

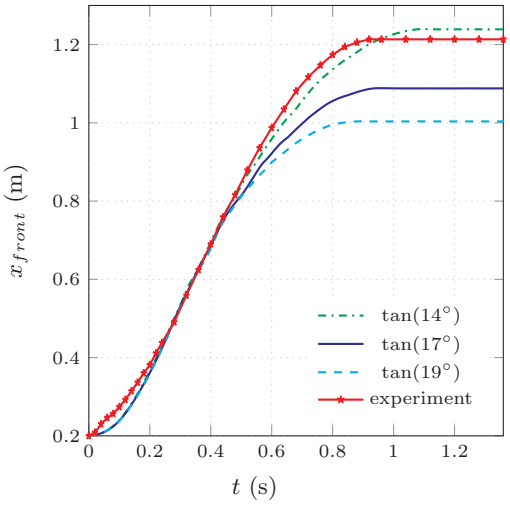

Figure 17: Time evolution of the front position during the spreading of the granular mass. The front stops at $t = 0.9$ s and the upper part of the basal deposit grows up to $t = 1.36$ s where a steady state is reached. Results obtained with three different values of the basal friction angle (14°, 17° and 19°) are shown and compared with the experimental result.

The fact that the simulations with tan(17°) and tan(19°) match fairly well the experiment suggests that the assumption of a particle-wall friction coefficient of tan(19°) based on the test with the sliding block is reasonable. In experiments, however, friction occurs also at the lateral walls. The effect of the lateral walls is probably small because the height of the flowing layer becomes increasingly small compared to the channel width when the granular mass spreads, but it is certainly non-negligible. If lateral friction was considered in the simulations then at given friction coefficient the runout distance, for instance, would be smaller than observed in the present simulations. In consequence, lower coefficients would be required to match the experiment. This suggests that the particle-wall friction coefficient is close to but less than tan(19°). A possible explanation is that the particles at the flow base in the experiment may have some rolling component whereas the particles glued at the base of the solid block used for the test are truly static.

Also, according to the discussions in sections 4.1.3 and 4.1.4, the prediction of the runout distance could probably be improved by using a finer spatial resolution and/or a smaller value of the viscosity. Due to a larger computational cost, simulations with smaller values of η_s were not performed for this experiment. Remember that the time step had to be divided by two in section 4.1.4, for $\eta_s \leq 0.1$ Pa s. As a summary, the value tan(17°) is a good compromise and is retained for the simulations further discussed. Note that for this initial column, the final deposit clearly has two slopes: a first one of 7° for $x \geq 0.5$ m up to the front of the granular mass and a steeper one of 29° for $x \leq 0.35$ m. These slopes are well approximated by all simulations (see figure 16). As for the previous experiment, the level-set method is able to predict a thin deposit near the front: the angle between the surface of the deposit and the flat horizontal plate is very small. Indeed, we respectively find 2.85°, 3.5° and 4.85° for increasing values of the basal friction compared to 2.5° for the experiment. As a summary, dependence of the results upon the basal friction is weak and the three different results are more than acceptable when compared to the experiment.

By looking at the time evolution of the front of the granular mass during the collapse shown on figure 17, we deduce as in section 4.1.2 that the dynamics of the slump can be divided in four phases: a short acceleration phase followed by a time period where the propagation speed of the front is constant, then a deceleration phase and finally a long time period with a very slow motion until the flow stops. Due to the fact that effects of the gate is not accounted for in our simulations, a small time delay in the sliding of the front is visible during the acceleration period, that is for $t \in [0, 0.15]$

s. In the second phase, that is $t \in [0.15, 0.5]$ s, all the three basal friction coefficients provide curves that can not be differentiated and are superposed with the experimental one until the deceleration phase. The propagation speed is here better approximated than for the shorter column shown on figure 6. However, simulations for the different values of the basal friction coefficient have slightly different deceleration phases as they reach different runout distances.

4.2.3 Numerical results obtained with 17° as basal friction angle: comparison with experiment.

According to the previous discussion, the basal friction coefficient is chosen equal to $\kappa_{\rm b} = \tan(17^\circ)$ for further analysis. On figure 18, profiles of the granular mass computed with the DP-model are shown at different times during the collapse and compared with the experimental one. Except during the acceleration phase, *i.e.* for $t \leq 0.16$ s, where the experimental front is further advanced than the numerical one, the numerical profiles are in good agreement with the experimental ones. During the deceleration phase ($t \geq 0.4$ s), the granular mass consists of two areas with different surface slopes: a bend on the interface occurs at $x \approx 0.4$ cm.

At the final (stationary) time $t = 1.36$ s, the slope of the interface at the back wall is particularly well approximated by the numerical simulation. In the ranges $x \in [0, 0.3]$ m and $x \in [0.5, 1.1]$ m, both profiles are almost identical while the profile predicted by the numerical simulation is slightly below the experimental curve for $x \in [0.3, 0.5]$ m. By looking at the norm of the velocity field $|\boldsymbol{u}|$ (in $\mathrm{m\,s^{-1}}$) (in figure 18) and the strain rate $|\boldsymbol{D}(\boldsymbol{u})|$ (in $\mathrm{s^{-1}}$) (in figure 19), a basal deposit growing with time is clearly visible. Also, as already observed for the 0.7 aspect ratio column, the motion takes place in a thin surface layer. The velocity takes its largest values in a narrow zone behind the front. The maximum velocity at the front is of the order of 1.6 m $\mathrm{s^{-1}}$.

Both the pressure (figure 20) and the strain rate (figure 19) exhibit short wave oscillations during the whole collapse. As this was the case for the 0.7 aspect ratio column, despite these oscillations the simulations remain stable and the pressure is bounded by $\rho_{\rm s} g H_c \approx 6082$ Pa. As it was discussed in section 4.1.2, pressure oscillations are well-known for the DP-rheology and are related to the ill-posedness of the model. Nevertheless, the DP-model permits us to obtain accurate simulations of the collapse of granular columns, which is somehow disturbing from a mathematical point of view.

4.2.4 Structure of the granular flow and characteristics of the deposit

From measurements and analyses of experiments, it has been shown in Roche *et al.* (2010) and Roche (2012) that the flow of a granular material during the collapse of column consists of a basal deposit growing at a nearly constant rate and overlain by a moving layer with a sliding head where most of the flow motion occurs. Following Roche (2012), we aim to characterise both the basal deposit and the flow head by computing several related quantities and then by comparing numerical and experimental results. It was somewhat difficult to find a good numerical criteria in order to define the deposit zone and the moving layer. We used the velocity norm as discriminant quantity and defined the basal deposit as the region inside the granular mass where the velocity norm was below 1% of its maximum value. On figure 21 the granular mass, at any time during its spreading, is schematically split into a basal deposit extending from the back wall of the channel up to the distance $L_d + L_c$ where L_d is the length of the deposit measured from the gate, which is located at $x = L_c$ from the origin. The flow occurs in the layer above the basal deposit and below the interface with ambient air: the dotted area on figure 21. The foremost part of this layer sliding on the bottom wall is named the head of the granular flow and is characterised by the length L_h, which is defined by: $L_h = L - L_d$ where L is the total length of the granular mass measured from the gate. As observed in the experiment, the length L_h of the sliding head increases, then reaches a plateau and finally decreases as the time evolves (see figure 22, left curve). Note that a better agreement

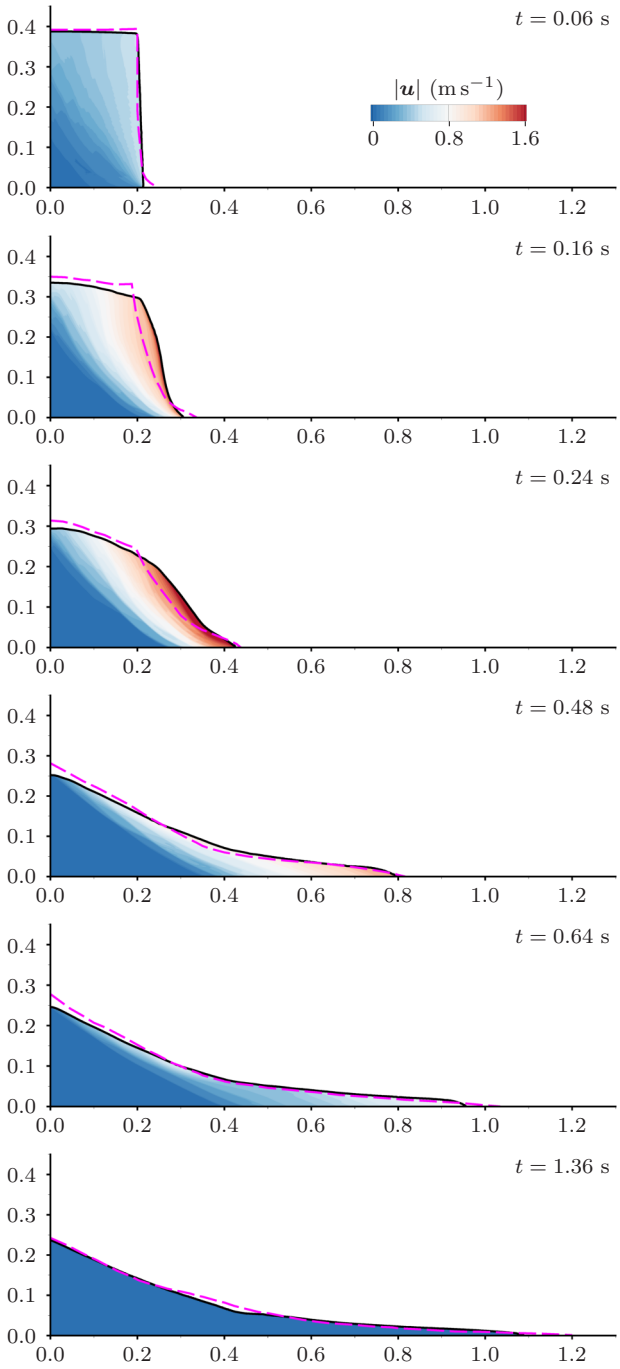

Figure 18: Comparison between numerical (black solid curve) and experimental (pink dashed curve) results of the collapse of a granular mass. The colour scale corresponds to the velocity Euclidean norm $|\boldsymbol{u}|$ (in m s^{-1}) computed by using the DP-rheology. The numerical resolution is $h = 1.796875 \times 10^{-3}$ m ($n = 256$), the computational domain is $\Omega = (0, 1.38) \times (0, 0.46)$ and the basal friction coefficient is $\kappa_{\mathrm{b}} = \tan(17°)$.

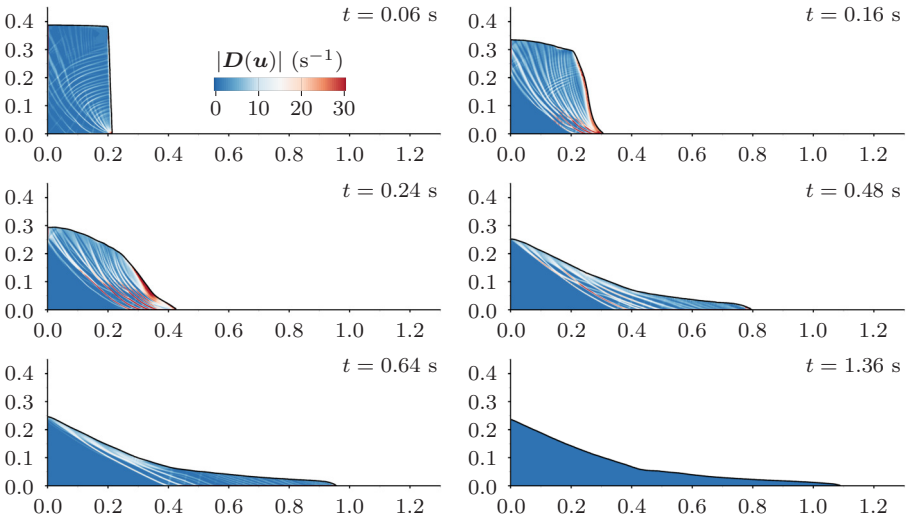

Figure 19: Strain rate $|\boldsymbol{D}(\boldsymbol{u})|$ (in s^{-1}) at different times during the granular mass slump simulated with the DP-rheology. The numerical resolution is $h = 1.796875 \times 10^{-3}$ m ($n = 256$), the computational domain is $\Omega = (0, 1.38) \times (0, 0.46)$ and the basal friction coefficient is $\kappa_{\mathrm{b}} = \tan(17°)$.

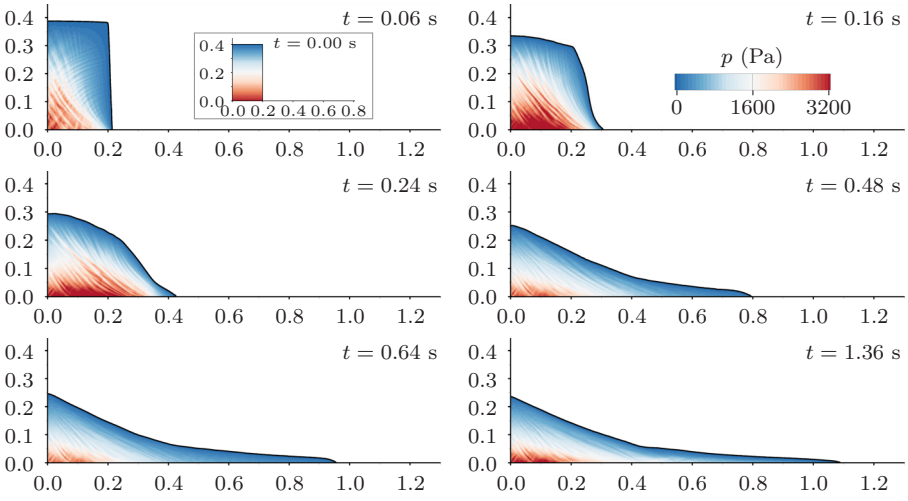

Figure 20: Pressure p (in Pa) at different times during the granular mass slump simulated with the DP-rheology. The initial static state at $t = 0$ s is also shown. Note that a different scale is used for the initial pressure, which takes a larger maximum value (≈ 6082 Pa). The numerical resolution is $h = 1.796875 \times 10^{-3}$ m ($n = 256$), the computational domain is $\Omega = (0, 1.38) \times (0, 0.46)$ and the basal friction coefficient is $\kappa_{\mathrm{b}} = \tan(17°)$.

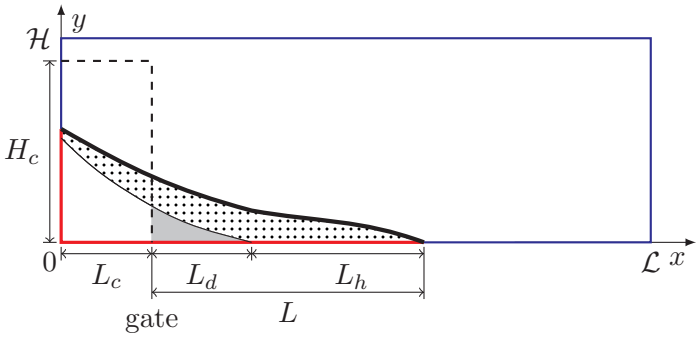

Figure 21: Granular flow structure determined by the upper flow surface (bold black) and the interface with the basal deposit (thin black). The wall contact surface between the granular flow and the channel is shown in red. The dashed line represents the initial granular column. The length of the granular mass on the x-axis, measured from the gate, L is decomposed into the basal deposit length L_d and the length of the sliding head L_h.

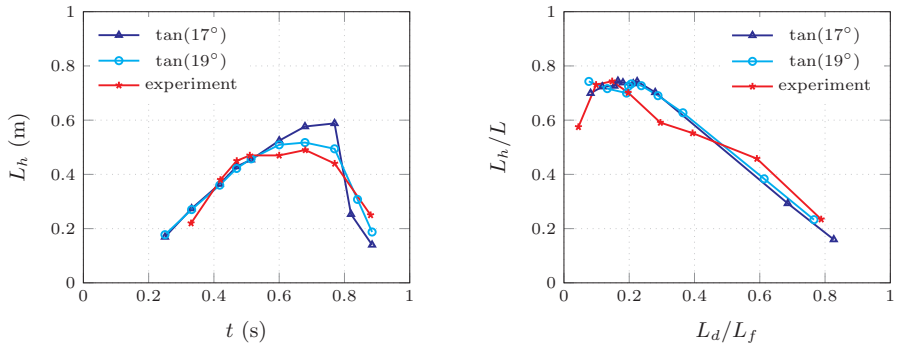

Figure 22: Structure of the granular flow for $H_c/L_c = 2$. Time evolution of the length of the sliding head L_h (left). L_h/L represented as a function of the ratio L_d/L_f (right) where L_f is the runout distance. Results obtained with basal coefficients tan(17°) and tan(19°) are compared with values measured from the experiment.

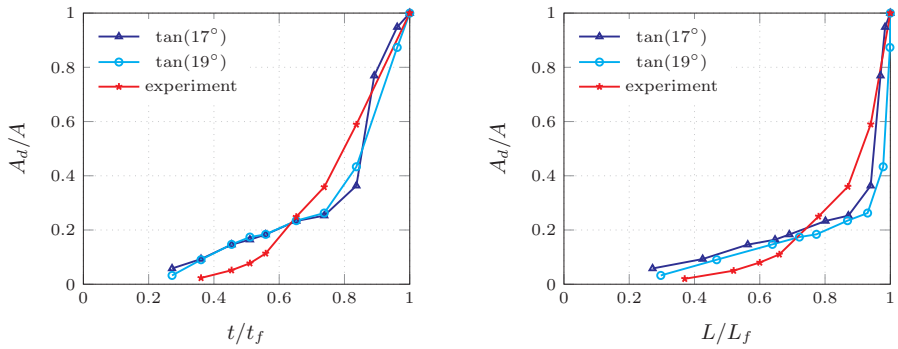

Figure 23: Structure of the granular flow for $H_c/L_c = 2$. Deposit area A_d (gray region on figure 21) normalised by the total area A of the granular flow outside the reservoir as function of normalised time (left) and position (right). The final time is $t_f = 1.36$ s, *i.e.* where the experiment ends and L_f is the runout distance. Results obtained with basal coefficients tan(17°) and tan(19°) are compared with values measured from the experiment.

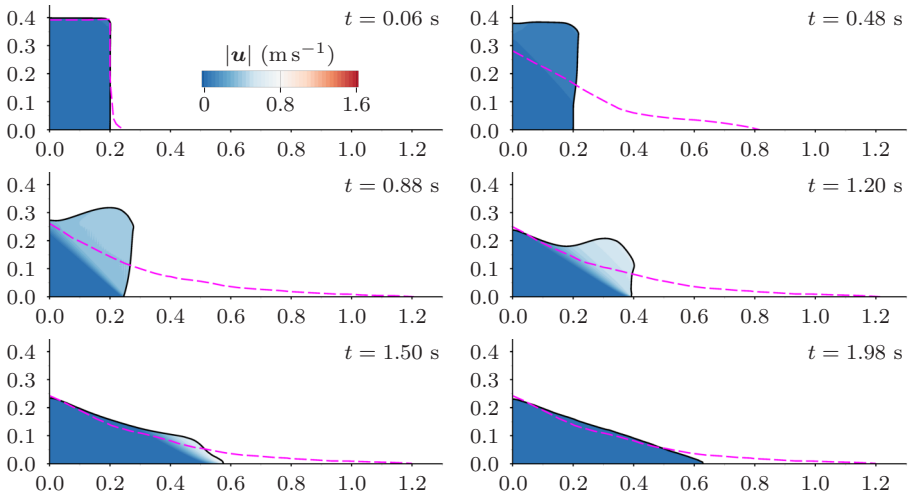

Figure 24: Comparison between numerical (black solid curve) and experimental (pink dashed curve) results of the collapse of a granular mass. The colour scale corresponds to the velocity Euclidean norm $|\boldsymbol{u}|$ (in m s^{-1}) computed by using the HP-rheology. The numerical resolution is $h = 3.90625 \times 10^{-3}$ m ($n = 128$), the computational domain is $\Omega = (0, 4) \times (0, 0.5)$ and the basal friction coefficient is $\kappa_{\mathrm{b}} = \tan(19°)$.

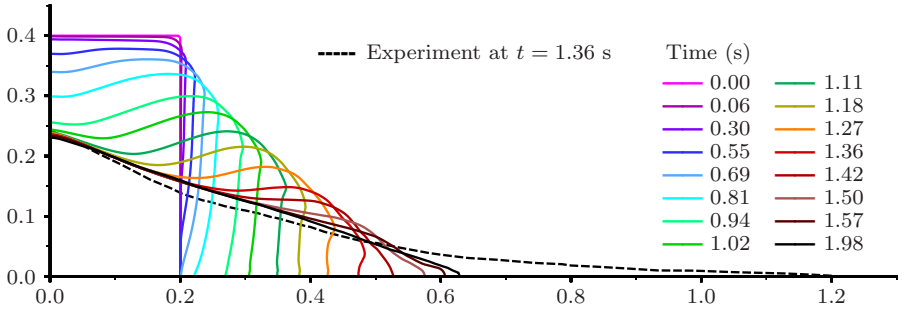

Figure 25: Profiles of the granular mass at different times, predicted by the HP-model. The numerical resolution is $h = 3.90625 \times 10^{-3}$ m ($n = 128$), the computational domain is $\Omega = (0, 4) \times (0, 0.5)$, and the basal friction coefficient is $\kappa_{\mathrm{b}} = \tan(19°)$.

with the experimental curve is found when the basal coefficient is set to $\tan(19°)$. Also shown on figure 22 (right curve) is the ratio L_h/L, which decreases linearly with the distance L_d/L_f, where L_f is the runout distance reached by the granular mass at stationary state, *i.e.* when the flow motion ends (at time $t = t_f$). A very good agreement with the experimental values is obtained both with $\tan(17°)$ and $\tan(19°)$.

The basal deposit can also be characterised by the area A_d (gray area on figure 21), which is equal to the area of the deposit in the channel. The fraction of the basal deposit area A_d over the area A of the whole granular material in the channel slowly increases during the stage of constant speed propagation, that is for $t \in (t_1, t_2)$, reaching approximately $20 - 25\%$ (see figures 23). During the last stages, A_d/A increases more rapidly until motion in the granular mass stops, so that $A_d = A$. Note that the basal friction coefficient has a small influence on the results which are in good agreement with the experimental values both with $\tan(17°)$ and $\tan(19°)$.

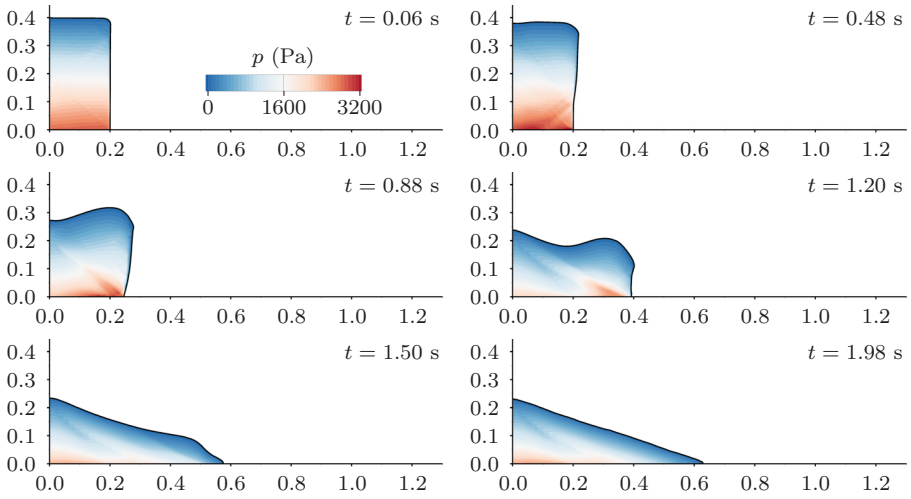

Figure 26: Pressure p (in Pa) at different times during the granular mass slump simulated with the HP-model. The numerical resolution is $h = 3.90625 \times 10^{-3}$ m ($n = 128$), the computational domain is $\Omega = (0, 4) \times (0, 0.5)$ and the basal friction coefficient is $\kappa_b = \tan(19°)$.

4.2.5 The HP-rheology

As discussed previously (section 4.1.5), numerical simulations with the HP-model were performed in order to evaluate its ability to reproduce the flow dynamics and the final deposit characteristics for the collapse of the initial column with aspect ratio 2. As shown on figures 24 and 25, the HP-model fails to reproduce both the flow dynamics and the final deposit. The runout distance is underestimated by almost 50% though the height on the back wall is correctly predicted. Unlike what was obtained with the DP-model, the shape of the final deposit is wrong as the HP-model predicts a decrease of the granular mass with a constant slope ($\approx 17°$) while two different slopes should be found as mentioned in section 4.2.2. As already mentioned, the strength of the yield stress defined as proportional to the hydrostatic pressure is stratified and far too strong, thus inhibiting motion of the right foot of the column, which destabilises in a non-physical manner from above. The simulation is stopped at $t = 1.98$ s, because at this time both the velocity and strain-rate norms are sufficiently small to consider that a steady state has been reached. In contrast in the experiment, the final time is found to be $t_f = 1.36$ s. As expected and due to the well–posedness of the HP-model, the computed dynamic pressure has no visible small-scale oscillations as the ones produced by the DP-model (see figure 26). Note that the computational domain in this case was extended in the horizontal direction up to $L = 4$ m (instead of 1.38 m for simulations with the DP-model) for the following reason. Between $t = 1.2$ s and $t = 1.5$ s, the velocity speed in the ambient air suddenly and locally increases close the front. This results in a fast and small vortex sliding along the horizontal axis, visible on figure 27 for $x \approx 0.8$ m. If the computational domain is not long enough, so that dissipation of this vortex occurs before it reaches the domain exit, numerical instabilities may develop and eventually lead to a blow-up.

5 Summary and conclusions

In an effort to improve the modeling of granular flows as a continuum and in order to go further than previous numerical studies, the efficiency and behaviour of the viscoplastic rheology with pressure-dependent threshold have been investigated in this study through the comparison with experiments and other (published) numerical results when available. Two experiments of the collapse of columns of glass beads, with diameters respectively equal to 0.7 mm and 0.08 mm, and

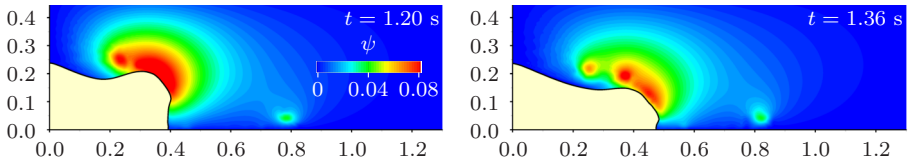

Figure 27: Stream function in the ambient air, at times $t = 1.20$ s and 1.36 s, obtained with the HP-model. The structure in the neighbourhood of $x = 0.8$ m moves right, artificially grows and leads to a numerical instability if the computational domain is not long enough. Here, $\Omega = (0, 4) \times (0, 0.5)$.

aspect ratios respectively equal to 0.7 and 2, were considered. For the latter, numerical simulations are presented and analysed for the first time. In that case, depth-averaged models are likely to be less accurate as the aspect ratio exceeds the unity.

Two viscoplastic models have been retained for this study. They both have constant viscosity but different yield stress: the Drucker-Prager (DP) yield stress is proportional to the dynamic pressure of the flow while the yield stress in the hydrostatic pressure (HP) model depends on the static pressure derived from the flow height. The HP-model is known to be well–posed while the DP-model is ill-posed and leads to small-scale instabilities. Nevertheless, the latter has been shown to be able to reproduce the main features of experimental granular mass collapse presented in previous publications (Ionescu *et al.*, 2015; Martin *et al.*, 2017). One of the objective of this paper was to evaluate the efficiency of the HP-model by comparing numerical simulations with experiments and with DP-model simulations.

A level-set formulation for the momentum and mass conservation equations is used. The interface between the granular material and the ambient air is tracked with high-order schemes and with an appropriate treatment near boundaries. Coulomb friction boundary conditions are applied on the walls so that sliding of the front during the spreading of the granular mass is allowed. The non-differentiability of the yield stress rheology is handled with a projection formulation allowing a computation of the plastic part of the stress tensor through a fixed point procedure having a geometric convergence. Using the level-set method for the collapse of a granular column is challenging as this method is known to have difficulties to reproduce accurately the sliding of a front on a wall. In the present study, the level-set method coupled with Coulomb friction conditions on the horizontal wall is able to capture a very thin front of the granular mass, almost as thin as the experimental one.

Despite its ill-posedness, the DP-model provides accurate predictions of the dynamics, the runout distance and the shape of the granular mass during the collapse for both experiments. In the case with aspect ratio 0.7, the mesh size was decreased down to the diameter of the glass beads (0.7 mm) and a remarkably accurate prediction of the interface between the granular flow and the ambient air is recovered. Sensitivity of the results with respect to the viscosity is also investigated. When the viscosity is decreased, convergence of the numerical results is observed and more accurate runout distances are obtained. In the area close to the vertical back wall, the numerical results perfectly fit the experimental ones. The four different stages characterising granular mass spreading and observed in experiments are well predicted by the DP-model. Also, the granular mass during its collapse is known to separate into a basal deposit over which flows a thin layer of materials with a sliding head. For the taller initial column, the internal dynamics of the granular mass, namely the static-mobile interface between the basal deposit and the flowing layer, is well captured and a good agreement with the experiment is found. We present for the first time numerical quantification of the static and moving parts of a granular material during its spreading.

On the other hand, the well-posed HP-model completely fails to reproduce the dynamics of the granular mass collapse. Intermediate profiles are not physically relevant because the vertically stratified yield stress is too strong and inhibits sliding of the front, so that the granular column

destabilises from the top. Surprisingly, an acceptable final deposit is predicted for an initial column with aspect ratio 0.7, although the runout distance is underestimated, but this is no longer the case when the aspect ratio exceeds the unity.

In order to develop further the present work, columns with larger aspect ratios could be considered and simulations with finer resolutions could be investigated in the case of beads smaller than 0.08 mm. We plan also to extend our code to three-dimensional geometries, possibly with lateral walls. Interesting test cases are the collapse of 3D columns and fast flows on inclined planes for which lateral walls may have non negligible effects (see Brodu *et al.*, 2015).

This work is supported by the French Government Laboratory of Excellence initiative n°ANR-10-LABX-0006, by the French National Research Agency (ANR) RAVEX project, and by the French National Joint Research Program TelluS of INSU and INSMI CNRS (National Centre for Scientific Research). This is Laboratory of Excellence ClerVolc contribution number 402. The numerical simulations have been performed on a DELL cluster with 32 processors Xeon E2650v2 (8 cores), 1 To of total memory and an infiniband (FDR 56Gb/s) connecting network.

Declaration of Interests. The authors report no conflict of interest.

References

Balay, S., Abhyankar, S., Adams, M.F., Brown, J., Brune, P., Buschelman, K., Dalcin, L., Dener, A., Eijkhout, V., Gropp, W.D., Kaushik, D., Knepley, M.G., May, Dave A., McInnes, Lois Curfman, Tran Mills, R., Munson, T., Rupp, K., Sanan, P., Smith, B.F, Zampini, S., Zhang, H. & Zhang, H. 2018*a* PETSc users manual. *Tech. Rep.* ANL-95/11 - Revision 3.10. Argonne National Laboratory.

Balay, S., Abhyankar, S., Adams, M.F., Brown, J., Brune, P., Buschelman, K., Dalcin, L., Dener, A., Eijkhout, V., Gropp, W.D., Kaushik, D., Knepley, M.G., May, Dave A., McInnes, Lois Curfman, Tran Mills, R., Munson, T., Rupp, K., Sanan, P., Smith, B.F, Zampini, S., Zhang, H. & Zhang, H. 2018*b* PETSc Web page. `http://www.mcs.anl.gov/petsc`.

Balmforth, N. J. & Kerswell, R. R. 2005 Granular collapse in two dimensions. *Journal of Fluid Mechanics* **538**, 399–428.

Barker, T. & Gray, J.M.N.T. 2017 Partial regularisation of the incompressible $\mu(I)$-rheology for granular flow. *J. Fluid Mech.* **828**, 5–32.

Barker, T., Schaeffer, D.G., Bohórquez, P. & Gray, J.M.N.T. 2015 Well-posed and ill-posed behaviour of the $\mu(I)$-rheology for granular flow. *J. Fluid Mech.* **779**, 794–818.

Brodu, N., Delannay, R., Valance, A. & P., Richard 2015 New patterns in high-speed granular flows. *J. Fluid Mech.* **769**, 218–228.

Chalayer, R., Chupin, L. & Dubois, T. 2018 A bi-projection method for incompressible bingham flows with variable density, viscosity, and yield stress. *SIAM J. Numer. Anal.* **56** (4), 2461–2483, arXiv: https://doi.org/10.1137/17M113993X.

Chang, Y.C., Hou, T.Y., Merriman, B. & Osher, S. 1996 A level set formulation of eulerian interface capturing methods for incompressible fluid flows. *J. Comput. Phys.* **124**.

Chorin, A.J. 1968 Numerical solution of the Navier-Stokes equations. *Math. Comp.* **22**, 745–762.

Chupin, L. & Dubois, T. 2016 A bi-projection method for Bingham type flows. *Comput. Math. Appl.* **72** (5), 1263–1286.

Chupin, L. & Mathé, J. 2017 Existence theorem for homogeneous incompressible Navier–Stokes equation with variable rheology. *Eur. J. Mech. B-Fluid* **61**, 135–143.

Crosta, G. B., Imposimato, S. & Roddeman, D. 2009 Numerical modeling of 2-d granular step collapse on erodible and nonerodible surface. *J. Geophys. Res. Earth Surface* **114** (F3).

Delannay, R, Valance, A, Mangeney, A, Roche, O & Richard, P 2017 Granular and particle-laden flows: from laboratory experiments to field observations. *J. Phys. D Appl. Phys.* **50** (5), 053001.

Della Rocca, G. & Blanquart, G. 2014 Level set reinitialization at a contact line. *J. Comput. Phys.* **265**, 34–49.

GDR MiDi 2004 On dense granular flows. *Eur. Phys. J.* **E14**, 341–365.

Girolami, L., Hergault, V., Vinay, G. & Wachs, A. 2012 A three-dimensional discrete-grain model for the simulation of dam-break rectangular collapses: comparison between numerical results and experiments. *Granul. Matter* **14** (3), 381–392.

Glowinsky, R., Lions, J.-L. & Trémolières, R. 1981 *Numerical Analysis of Variational Inequalities*. North-Holland, Amsterdam.

Gottlieb, S. & Shu, C.-W. 1998 Total variation diminishing Runge-Kutta schemes. *Math. Comp.* **67** (221), 73–85.

Guermond, J.L., Minev, P. & Shen, J. 2006 An overview of projection methods for incompressible flows. *Comput. Methods Appl. Mech. Eng.* **195** (44), 6011 – 6045.

Gueugneau, V., Kelfoun, K., Roche, O. & Chupin, L. 2017 Effects of pore pressure in pyroclastic flows: Numerical simulation and experimental validation. *Geophys. Res. Lett.* **44** (5), 2194–2202.

Harlow, F.H. & Welch, J.E. 1965 Numerical calculation of time-dependent viscous incompressible flow of fluid with free surface. *Phys. Fluids* **12** (8), 2182–2189.

Ionescu, I.R., Mangeney, A., Bouchut, F. & Roche, O. 2015 Viscoplastic modeling of granular column collapse with pressure-dependent rheology. *J. Non-Newt. Fluid* **219**, 1–18.

Jiang, G.-S. & Peng, D. 2000 Weighted eno schemes for hamilton-jacobi equations. *SIAM J. Sci. Comput.* **21** (6).

Jop, P.and Forterre, Y. & Pouliquen, O. 2006 A constitutive law for dense granular flows. *Nature* **441**, 727–730.

Kerswell, R. R. 2005 Dam break with coulomb friction: A model for granular slumping? *Phys. Fluids* **17** (5), 057101.

Lacaze, L. & Kerswell, R.R. 2009 Axisymmetric granular collapse: A transient 3d flow test of viscoplasticity. *Phys. Rev. Lett.* **102**, 108305.

Lacaze, L., Phillips, J.C. & Kerswell, R.R. 2008 Planar collapse of a granular column: Experiments and discrete element simulations. *Phys. Fluids* **20** (6), 063302.

Lagrée, P., Staron, L. & Popinet, S. 2011 The granular column collapse as a continuum: Validity of a two-dimensional Navier–Stokes model with a $\mu(I)$-rheology. *J. Fluid Mech.* **686**, 378–408.

Larrieu, E., Staron, L. & Hinch, E.J. 2006 Raining into shallow water as a description of the collapse of a column of grains. *J. Fluid Mech.* **554**, 259–270.

Liu, Y., Balmforth, N.J., Hormozi, S. & Hewitt, D.R. 2016 Two–dimensional viscoplastic dambreaks. *J. Non-Newt. Fluid* **238**, 65 – 79.

Mangeney, A., Roche, O., Hungr, O., Mangold, N., Faccanoni, G. & Lucas, A. 2010 Erosion and mobility in granular collapse over sloping beds. *J. Geophys. Res. Earth Surface* **115** (F3).

Mangeney-Castelnau, A., Bouchut, F., Vilotte, J. P., Lajeunesse, E., Aubertin, A. & Pirulli, M. 2005 On the use of saint venant equations to simulate the spreading of a granular mass. *J. Geophys. Res. Solid Earth* **110** (B9).

Martin, N., Ionescu, I. R., Mangeney, A., Bouchut, F. & Farin, M. 2017 Continuum viscoplastic simulation of a granular column collapse on large slopes: $\mu(I)$ rheology and lateral wall effects. *Phys. Fluids* **29** (1), 013301.

Min, C. 2010 On reinitializing level set functions. *J. Comput. Phys.* **229**.

Osher, S. & Fedkiw, R. 2003 *Level Set Methods and Dynamic Implicit Surfaces*, *Applied Mathematical Sciences*, vol. 153. Springer-Verlag, New-York.

Roche, O. 2012 Depositional processes and gas pore pressure in pyroclastic flows: an experimental perspective. *B. Volcanol.* **74** (8), 1807–1820.

Roche, O., Montserrat, S., Niño, Y. & Tamburrino, A. 2010 Pore fluid pressure and internal kinematics of gravitational laboratory air-particle flows: Insights into the emplacement dynamics of pyroclastic flows. *J. Geophys. Res. Solid Earth* **115** (B9), B09206.

Schaeffer, D.G. 1987 Instability in the evolution equations describing incompressible granular flow. *J. Differ. Equations* **66** (1), 19–50.

Schaeffer, D.G. & Pitman, E.B. 1988 Ill-posedness in three-dimensional plastic flow. *Commun. Pure Appl. Math.* **41** (7), 879–890.

Shu, C.-W. & Osher, S. 1988 Efficient implementation of essentially non-oscillatory shock-capturing schemes. *J. Comput. Phys.* **77** (2), 439–471.

Sussman, M., Fatemi, E., Smereka, P. & Osher, S. 1998 An improved level set method for incompressible two-phase flows. *Comp. Fluids* **27** (5-6).

Sussman, M., Smereka, P. & Osher, S. 1994 A level set approach for computing solutions to incompressible two-phase flow. *J. Comput. Phys.* **114**.

Sussman, M., Smith, K.M., Hussaini, M.Y., Otha, M. & Zhi-Wei, R. 2007 A sharp interface method for incompressible two-phase flows. *J. Comput. Phys.* **221** (2).

Temam, R. 1969 Sur l'approximation de la solution des équations de Navier-Stokes par la méthode des pas fractionnaires. II. *Arch. Rational Mech. Anal.* **33**, 377–385.